ABSTRACT

Classification of Human Body Activities Using Low Profile Wearable Antennas

Bin Xu, Ph.D.

Mentor: Yang Li, Ph.D.

Monitoring human body activities has long been of interests because of their important applications in human–computer interfacing, virtual control, computer gaming, and medical care industries etc. Traditional methods, such as Doppler radar, depth camera, and wearable sensors, have been extensively studied and they showed good performance at certain scenarios. However, they also have their limitations in terms of their mobility and hardware cost.

In this dissertation, a new approach for monitoring body activities is introduced. It is based on the near-field perturbation effect of wearable antenna due to the body movements, which can cause the input impedance of wearable antenna to change. Compared with the above-mentioned radar or physical sensor-based methods, this approach does not only incur low cost and consume low power but also can provide high

classification accuracy. Moreover, users do not have to install or set up additional sensors because the antenna from a handheld device can be utilized.

In this study, three different kinds of wearable antennas are design, fabricated and tested on the human body. These antennas are the 3D printed folded cylindrical helix, folded cylindrical helix array, and textile patch antenna, not only can they be used for on-body and off-body communications, but they also can be used to monitor human activities. Several human dynamic experiments were conducted, including finger gestures, head and mouth activities, and arm motions. It is found that different body activities caused the S_{11} of wearable antennas to vary with unique patterns. Dynamic time warping algorithm classification results showed that more than 90% accuracy can be achieved to classify the 4 different finger motions performed in the experiment.

Classification of Human Body Activities Using Low Profile Wearable Antennas

by

Bin Xu, B.S., M.S.

A Dissertation

Approved by the Department of Electrical and Computer Engineering

____
Kwang Y. Lee, Ph.D., Chairperson

Submitted to the Graduate Faculty of
Baylor University in Partial Fulfillment of the
Requirements for the Degree
of

Doctor of Philosophy

Approved by the Dissertation Committee

____
Yang Li, Ph.D., Chairperson

____
Charles Baylis, Ph.D.

____
Liang Dong, Ph.D.

____
Jonathan Hu, Ph.D.

____
Randall Jean, Ph.D.

____
David Lin, Ph.D.

Accepted by the Graduate School
May 2018

____
J. Larry Lyon, Ph.D., Dean

Page bearing signatures is kept on file in the Graduate School.

TABLE OF CONTENTS

LIST OF FIGURES

LIST OF TABLES

LIST OF ABBREVIATIONS

CST – Computer Simulation Technology

DTW – Dynamic Time Warping

EBG – Electromagnetic Band-gap

ESPRIT – Estimation of Signal Parameters via Rotational Invariance Techniques

E-Texile – Electronic Textile

FCH – Folded Cylindrical Helix

NC – Nickel Copper

PLA – Polylactic Acid

SJ – Silver Jersey

VNA – Vector Network Analyzer

WBAN – Wireless Body Area Network

ACKNOWLEDGMENTS

I would like to express my sincerely gratitude to my advisor Dr. Yang Li, who provided me this great opportunity to do research at Baylor University. He not only taught me knowledges, but also provide all kinds of opportunities to improve my other skills, such presentation, writing, teaching and leadership skills, which I believe will benefit me through the rest of my life. I would also like to thank my parents and sister for their love and support during my Ph.D study. They kept motivating and inspiring me to do things that I love to do every day. I want to thank Dr. Cloud, Dr. Eike, Allyson Cliett, and Ling Ni for their great help in the textile antenna project. I need to acknowledge that the hard work of past and current students from Antennas and Propagation Lab: Fun Zhang, Willis Troy, Dong Xue, Drew Bresnahan, and Mary Leece, who have helped me a lot in the antenna measurements. I am grateful for Mr. Orr, Mr. Hynan, and Mrs. Simcik for their assistance during my school years. I wish to thank all my other dissertation committee: Dr. Baylis, Dr. Jean, Dr. Hu, Dr. Lin and Dr. Dong, for their guidance with my proposal and research.

This study is supported in part by funds from the National Science Foundation and the Collaborative Faculty Research Investment Program of Baylor University.

To my mother and father
For the love and support

CHAPTER ONE

Introduction and Background Information

The motivation of this dissertation originates from the recent development of wearable electronics and body centric wireless communications. The work of this dissertation gives a comprehensive study of classifying human body activities by using various wearable antennas.

1.1 Overview of Human Body Activities Monitoring

With the fast development of semiconductor industry and communication technologies, computer systems became much more lightweight and compact than before so that they can be worn on the human body and used to monitor human health conditions and body motions. Recognition of human body activities has a wide range of potential applications in the areas of wireless control, well-being and healthcare monitoring. Remote monitoring of hand and finger gestures can revolutionize the way of interaction between human and physical devices. For example, if a smart watch is able to recognize finger motions, we can interact with it without touching the tiny screen to avoid the inconvenience for touch control. Furthermore, if all the physical switches, scroll wheels and buttons can be eliminated and wirelessly controlled by hand gestures, it is much safer to control machines in a hazard environment.

Tracking people's daily activities can also help to maintain or improve people's life quality. One example is fitness tracking. Companies, such as Fitbit, Garmin, Apple, have developed their fitness tracking products, which can track people's walking and running steps, distances, calories burned, floors climbed as well as the sleep quality. Fig. 1.1 shows a working out shirt developed by Polo, which can detect the amount of calories burned and the intensity of activities during work out [1]. According to a recent international GFK survey [2] conducted online in 16 countries, about 1 in 3 people currently monitor their health or fitness via mobile applications, fitness band, or smartphone. Despite the above success in monitoring fitness, it still needs investigation to monitor mouth activities. In [3], Fang utilized the radio-based sensing approach to detect head and mouth-related activities, such as eating, drinking, coughing, and speaking. It is important to track how often people eat, drink, and cough as well as how much people speak every day. For example, tracking the amount of times that a person drink everyday can remind him to drink more or less frequently. Tracking people's head movement can remind them to shake their head after long-hour of working without head movement to relax their spine. This can help people not only form a more healthy diet habit, but also track people's health condition.

Fig. 1.1 Work-out shirt by Polo Ralph Lauren.

Monitoring human body activities also plays important roles in healthcare monitoring, including falling prevention and detection, rehabilitation, and sleep monitoring. One commonly happened high risk situation for elderly people is falling down. According to the Center for Disease Control and Prevention's report [4], around one-third of Americans over the age of 65 fall every year. Even in small country like Denmark, there were 13000 hospitalizations related with falls in 2005, and it is expected to rise to 24000 per year in 2030 [5]. About 10-20% falls cause serious injuries, and 5% leads to fractures [5]. The direct medical costs for fall injuries are $31 billion annually [6]. Being able to track daily gait patterns of elderly people is the key of preventing and detecting the falling, and can help them get appropriate treatment as early as possible.

1.2 Different Approaches for Monitoring Body Activities

Traditionally, there are three commonly used approaches to monitor human body activities: motion capture cameras, wearable sensors, and Doppler radars. The most widely used approach is to capture motions using depth cameras. In [7], a camera is used to capture the image of different hand gestures, as shown in Fig. 1.2. Then classification algorithms are applied to recognize different hand gesture. In [8], depth cameras are utilized to recognize eight activities: sitting, walking, going up, squatting, lying on a couch, falling, bending, and lying down. In [9], Auvinet developed a multiple-cameras network for detecting the falling action of elderly people living alone at home.

Fig. 1.2 Hand gesture detection by using a camera [7].

With recent proliferation of wireless body area networks, an alternate approach for recognizing human motions is to apply different kinds of wearable sensors. Gupta utilized an accelerometer to recognize walking, jumping, running, sit-to-stand, stand-to-sit activities [11]. Roy used smartphone accelerometer and gyroscope to monitor activities, such as sitting, standing, walking, running, lying and climbing stairs [12]. In [13], an accelerometer and gyroscope sensors are used to identify 37 arm, hand, and finger gestures with an average true positive rate of 98.11%. In [14], Hsieh proposed to use a waist-mounted tri-axial accelerometer to capture the human body movement. When the elderly people fall, the variations of angle between acceleration vector and three axes can help to characterize the fall action [14]. Ito [15] built a gait measurement and evaluation system, which consists seven wireless motion sensors worn on both legs and the waist, as is shown in Fig. 1.3. It can help to analyze elderly people's walking performance, thus help to prevent them falling. However, integrating these sensors into wireless wearable devices increases the cost and overall power consumption.

Fig. 1.3 Gait measurement and evaluation system [15].

The third approach of classifying human activities is to utilize Doppler radar, which can classify human activities based on micro-Doppler signatures regardless of the light condition. In [16], micro-Doppler information is used to classify running, walking, walking while holding a stick, crawling, boxing, and sitting still (as shown in Fig. 1.4), and an accuracy of 90.3% can be achieved. To increase the detection resolution, a 60 GHz Doppler radar is developed to detect hand or finger motions more precisely [17].

Fig. 1.4 Human body activity detection by Doppler radar [16].

1.3 Monitoring Body Activities Based on S_{11} Variation of Wearable Antenna

While previous studies can successfully recognize different body movements or hand gestures, there are some disadvantages for those three commonly used approaches that were discussed in 1.2. Firstly, the depth camera approach is limited with various light conditions and camera-facing angles. If the objective is tilted in a different angle, it will be difficult for the classification algorithm to recognize the movement. Furthermore, it is tricky to extracting background to get foreground object (human) [8]. Secondly, the sensor approach adds more hardware on our body, so the cost will be increased. The sensors will also drain the battery power, which is usually very limited on wearable electronics [13]. Thirdly, the Doppler radar approach is usually not wearable and not mobile. And it requires that the beam of the radar antenna must be directed to the target for data collection, so the detection range is limited [16]. Similar to the camera approach, the Doppler data is also sensitive to the radar-facing angle. Different angle generates different Doppler information even for the same movement.

Lately, it was found that the impedance variation of an on-body antenna, as a result of near field perturbations due to body movements, can be utilized to detect vital signals and classify various human activities [17-18]. In [18], a monopole was mounted on human chest (Fig. 1.5 (a)) and the S_{11} was recorded when a person performed different activities, as shown in Fig. 1.5 (b). It is found that different activities cause S_{11} to vary in different patterns. Compared to the above radar or physical sensors-based methods, this approach is not only of low cost and of low power consumption, but can provide high classification accuracy. Moreover, users do not have to attach or set up additional sensors because an antenna from a handheld device can be utilized. In spite of the success of monitoring different activities, the monopole used in the experiment is too big to be mounted on human body. So low profile wearable antennas needs to be designed for monitoring human activities.

1.4 Low Profile Wearable Antennas

Due to the fast-developing semiconductor industry, electronic devices have become much smaller, lighter, but much more powerful than ever before so that they can be carried in users' pockets or embedded in clothes [19-22]. Along this trend, a number of body-centric communication systems have been invented and utilized in medical, military, wellness industries [23-25]. Body-centric communication can be classified as off-body, on-body, and in-body communications [22]. Different communications have different requirements on the antenna performance. For on-body communication, the propagation channel is mainly on along the surface of the human body. So the antenna directivity is usually parallel to body surface. For off-body communication, the propagation channel is between the body and somewhere off the body. Thus, it requires the antenna directivity to be normal to the body surface. In-body communication requires the antenna implanted inside the body, which is beyond the scope of our study. The following subsections review the previous research works on wearable antennas for off-body and on-body communications.

1.4.1 Different Antenna Types

Most of the wearable antennas are derived from different types of conventional antennas, including monopole, loop antenna, microstrip antenna, slot antenna, PIFA antenna and so on. A number of studies have been conducted on the antenna performance change when these antennas are placed on human body [26-29]. It was found that the antenna performance may degrade significantly while operation in a close range with human body due to the high permittivity and high loss tangent of body tissues [22, 30].

In order to minimize the performance degradation for conventional single layer antenna, such as monopole, dipole, or loop antenna, some researcher came up with the idea of inserting a layer of electromagnetic bandgap (EBG) structures between body and the antenna in order to shield the near field of the antenna from coupling with body tissues [31-35]. Fig. 1.6 shows a compact EBG-backed planar monopole for wearable applications. It can achieve a 4.8% -10dB fractional bandwidth and a measured gain of 6.88 dBi [31]. The EBG structure not only isolates the antenna from body, but also enhances the radiation efficiency. In [35], Duan proposed a wearable slot antenna on top of an EBG structure. The antenna efficiency can be improved by 60% because of the EBG structure.

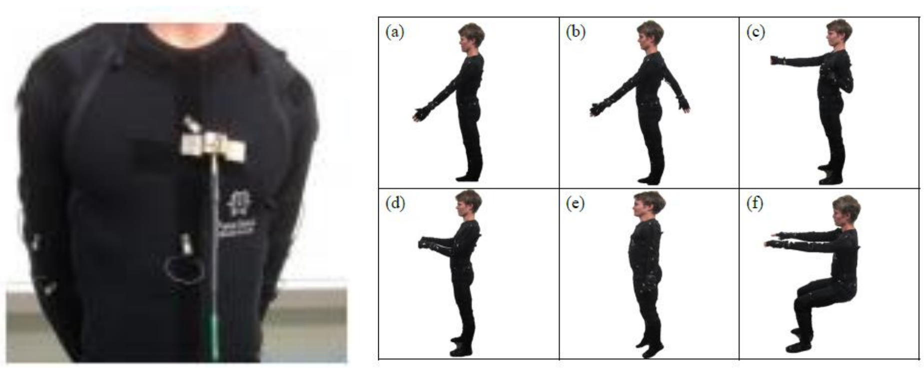

(a)

(b)

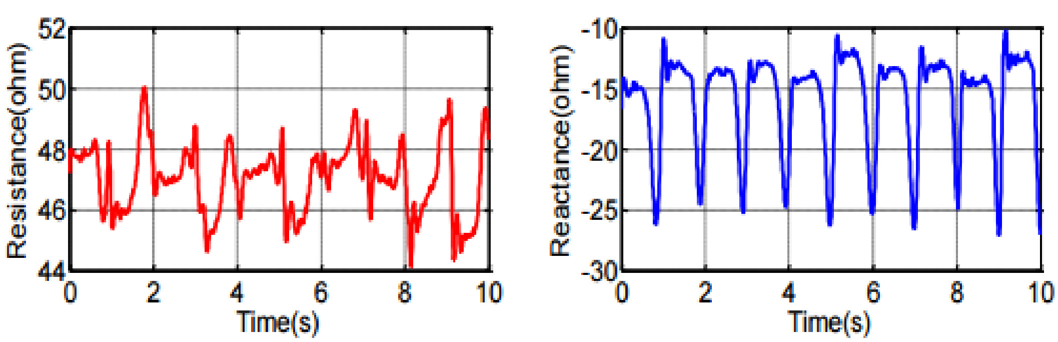

(c)

Fig. 1.5 (a) Monopole on chest (b) Different human activities (c) Impedance of monopole antenna when a subject performed activity a [8].

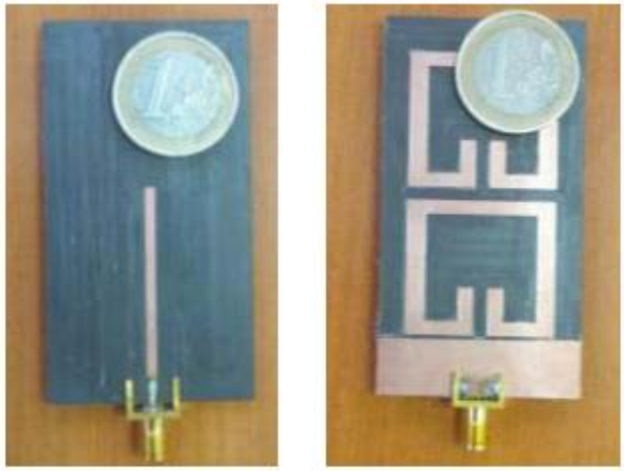

Fig. 1.6 EBG-backed monopole antenna for wearable applications [31].

In [36], the author designed a wearable patch antenna which can be integrated into a military beret for indoor/outdoor positioning system, as is shown in Fig. 1.7. Since the existence of ground plane, the antenna performance doesn't deviate much in proximity with human head. The specific absorption rate is well below the FCC guidelines.

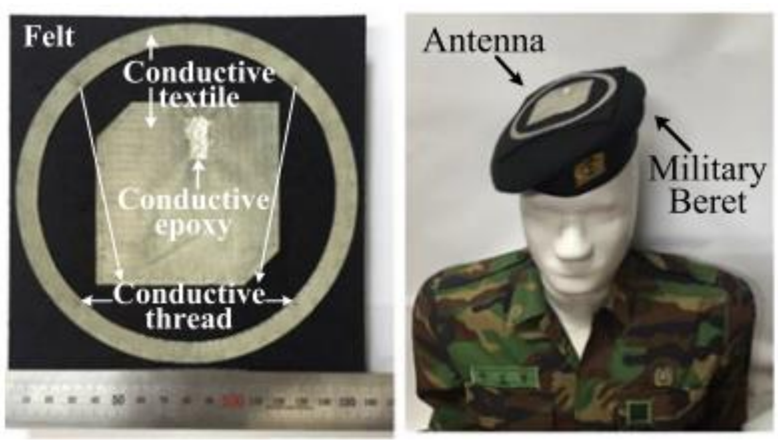

Fig. 1.7 Wearable patch antenna integrated into military berets [36].

1.4.2 Frequency Bands

For different applications, wearable antennas work at different frequency bands and different bandwidths. In terms of frequency bands, wearable antennas can be classified as narrow band antenna, wideband antenna, and multiband antenna.

A lot of studies have been conducted on narrow band wearable antennas. All the EBG backed wearable antennas discussed above are narrow band antennas [31-35], because the EBG structure are composed of resonating structures and there bandwidth are limiting. In [37], Ha proposed a u-slot patch antenna with reconfigurable beam steering as is shown in Fig. 1.8. Its bandwidth is 4.6% for VSWR less than 2. In [38], Paraskevopoulos designed a higher mode patch antenna for on-body communications. Its bandwidth is around 6% for S_{11} below -10 dB.

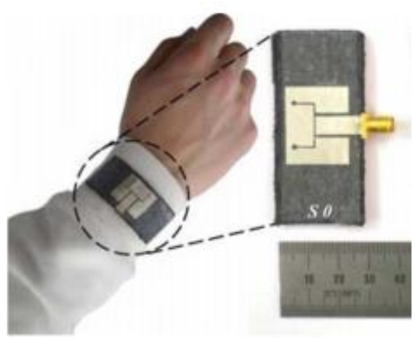

Fig. 1.8 U-slot wearable patch antenna [37].

Wideband wearable antennas are necessary for some applications [39-43], such as digital television broadcasting from 470 MHz to 770 MHz. There are several ways to realize wideband characteristics. Most of them have a size over 0.25 wavelength. One of the commonly used method to realize broadband is to create a multi-resonant structure [39, 42]. In [39], a broadband performance is achieved by adding an L shaped parasitic elements, as shown in Fig. 1.9. The T shaped monopole alone resonate at around 450 MHz. The high resonance frequency about 750 MHz was generated by the L-shaped parasitic elements. Another example, a broadband slot antenna, is also presented in [39]. By adding the arrow shaped slot, dual resonanceoccurred and the bandwidth for VSWR<2 was realized from 410 to 870 MHz. The fractional bandwidth is 72%. Another approach to realize broadband is to use frequency independent structure, such as biconical antenna, bow-tie antenna, spiral antenna and so on. In [43], a helmet mounted spiral antenna is designed. Fig. 1.10 shows the antenna configuration from top and side views. The VSWR remains below 2.5 from 230 MHz to 1 GHz. In this design, a metal ring is inserted below the antenna as a parasitic reflector to reduce the radiation toward head.

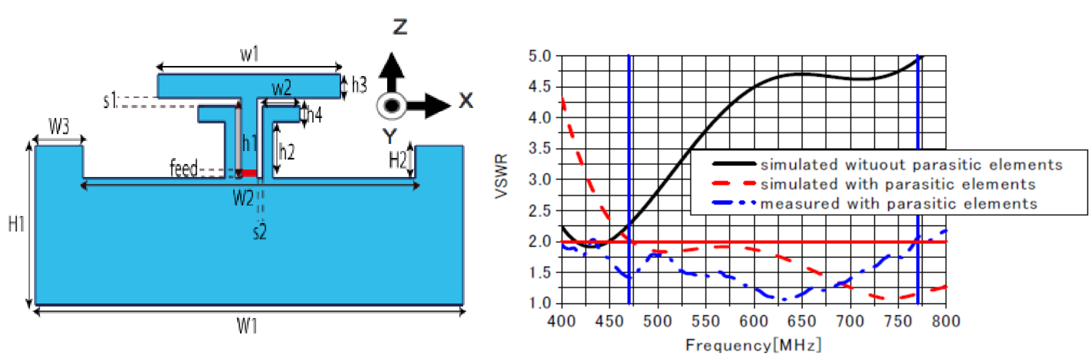

(a) (b)

Fig. 1.9 Multi-resonating wideband antenna (a) antenna prototype (b) VSWR [39].

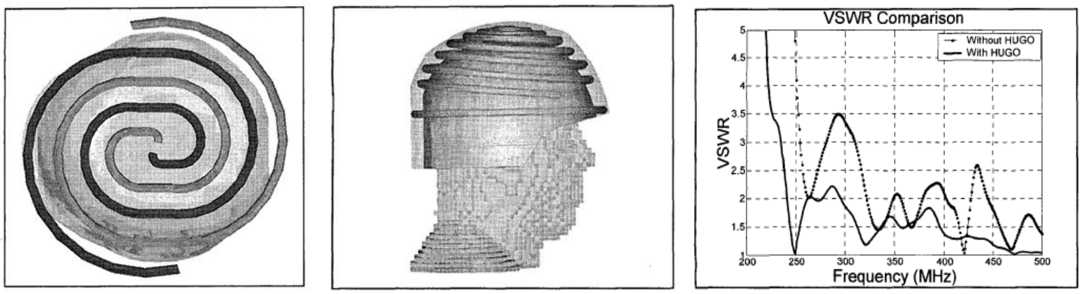

(a) (b) (c)

Fig. 1.10 Helmet mounted spiral antenna (a) Top view (b) Side view (c) VSWR [43].

In order to cover different communication bands, some dual band or multi-band wearable antennas were designed [44-48]. Fig. 1.11 shows a dual-band wearable button antenna [48]. It can work at 2.4 GHz band with a monopole type of radiation patter for on-body communication. It can also work at 5 GHz band with a broadside type of pattern for off-body communication. A high efficiency of 90% can be achieved by this antenna. Another example of multi-band wearable antenna is shown in Fig. 1.12. The antenna was designed for reception of digital television and wireless communications. It covers the DTV band, GSM-900, UMTS-LTE-advanced, WLAN and Wimax bands, as shown in Fig. 1.12 (c) [45]. The antenna performs well when it is worn on different locations of the human body.

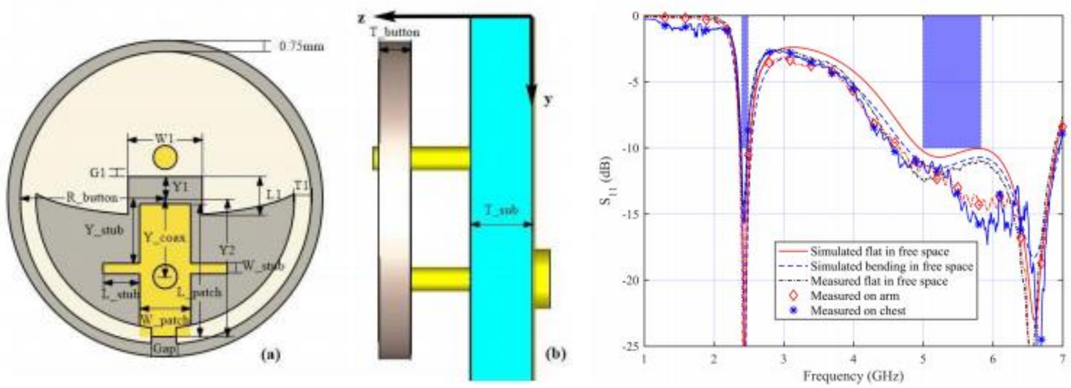

Fig. 1.11 Button shape dual-band wearable antenna [48].

1.4.3 Antenna Materials

In order to make the wearable antenna comfortable to wear, the antennas have to be flexible and conformal to the human body. This is different from the design of conventional antennas with rigid metal and substrates [49]. Accordingly, new materials and fabrication process were developed and applied to wearable antennas. In this subsection, we will review the conductive materials and substrate materials used for wearable antennas.

There are mainly three kinds of conductive materials for wearable antennas. First of all, pure metallic materials are used to fabricate wearable antennas, such as copper foil [50], silver paste [37] etc. These material can achieve similar conductivity as conventional metal used for conventional antennas, but can be more flexible than a traditional antenna. Another conductive material is metal-coated textiles [51-53]. These textiles are knitted or woven by conductive threads. Since they can sewed or embroidered directly into clothes, they are perfect for smart clothing applications. Fig. 1.13 shows some conductive textiles from LessEMF [54]. The third kind of conductive material is conductive ink, which consists of metal particles. It can be inkjet-printed on flexible substrates.

(a) (b)

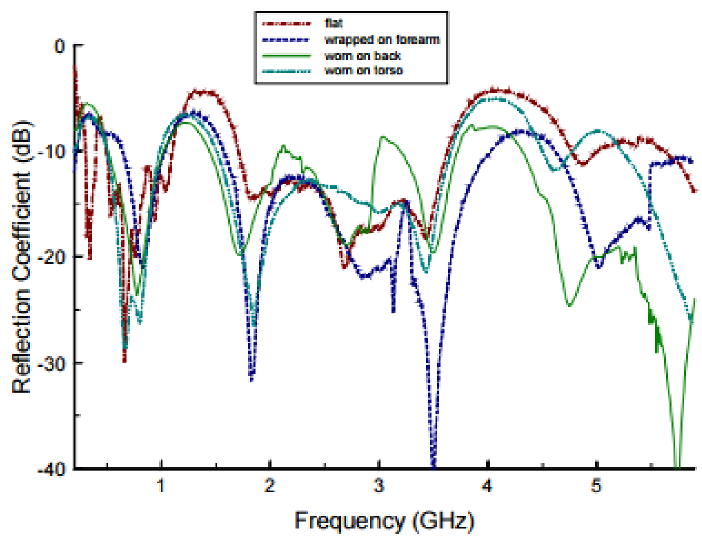

(c)

Fig. 1.12 Multi-band wearable antenna (a) front view (b) back view (c) S_{11} [45].

The substrates for wearable antennas are also desired to be light weight and flexible, so some of the flexible films are used for soft PCB processes [49], such as polyester films [55-56], polyimide films [57-58], and liquid crystal polymer films [59-60]. All these materials have low loss tangent and very good flexibility. For textile antenna, the nonconductive fabrics can be used as substrates, such as cotton, denim, polycot and so on. Table 1 lists the dielectric constant of some fabric materials [61].

Fig. 1.13 Some conductive fabrics from LessEMF [54].

Table 1. Dielectric constant of some fabric substrates.

Materials	Permittivity
Wash cotton	1.51
Curtain cotton	1.47
Polyester	1.44
Polycot	1.56
Jeans cotton	1.67
Floor spread	1.46

1.5 Objectives and Organization of the Dissertation

The objectives of my dissertation study are as follows. First, several kinds of wearable antennas are designed, fabricated, and measured. These antennas will work for on-body and off-body communications. Both narrow band and wideband antennas were designed. Second, the wearable antennas were utilized for dynamic on-body measurements, which include detecting different finger gestures, head and mouth activates and whole body activities. Finally, different classification algorithms were applied to recognize different body activities.

In Chapter Two, the design of two wearable antennas is presented, including a 3D printed folded cylindrical helix (FCH) antenna and a FCH antenna array. Their performance in the vicinity of the human body is examined. Chapter Three introduces the design of textile patch antenna and its performance under different harsh environmental and wear conditions. In Chapter Four, the wearable antennas utilized to monitor different body activities, which include finger motions, head, mouth activities, and arm motions. The measurement setup and results are presented. The classification algorithm and results are also presented. Chapter Five concludes the dissertation and introduces the future work.

CHAPTER TWO

Low Profile Wearable Folded Cylindrical Helix and Helix Array Design

Portion of this chapter published as two articles that I jointly authored:[85, 86]

In this chapter, two low profile wearable antennas are designed for on-body communication applications: a 3D printed folded cylindrical helix (FCH) and a FCH array.

2.1 3D Printed Folded Cylindrical Helix

Folded cylindrical helix (FCH) is an electrically small antenna, first introduced by S. Best [62]. Its height can be as low as 0.1λ. In this study, the FCH antenna was designed to be mounted on a human wrist and used for detecting finger motions. Two 4-arm, 1-turn FCH antennas are designed in open space at two center frequencies around 890MHz (antenna A) and 2.43 GHz (antenna B), respectively, using the approach presented by Best in [62]. The antenna dimensions are listed in Table 2, with the heights of the FCH are less than 0.05 wavelength at the resonating frequencies. Both antennas are simulatedusing CST and fabricated by using a 3D printer, Makerbot Replicator 2. As an example, Fig. 2.1 (a) and (b) show a simulation model and a fabricated prototype of the FCH antenna operating at 2.45 GHz. In the implementation, the holding mold used to support the FCH structure is made of polylactic acid (PLA) which has the dielectric constant of 1.4.

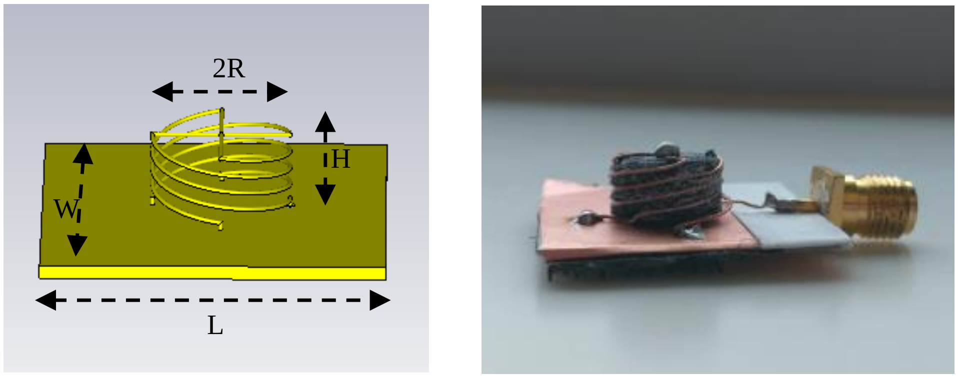

(a) (b)

Fig. 2.1 (a) Simulation model in CST and (b) side view of the fabricated 2.45 GHz FCH antenna.

Table 2 Dimensions of the FCH antennas.

Antenna	A	B
Resonance Frequency (MHz)	890	2430
Height H (mm)	14.4	5
Helix Radius R (mm)	14.4	5
Wire Radius (mm)	0.4	0.16
Ground Size W*L (mm)	40*40	25*25

First, we simulate and measure the reflection coefficients of antenna A and B in an open space, as shown in the Fig. 2.2 (a) and (b). The blue solid lines are the simulated results and the blue dashed lines are the measured results in free space. For both antennas, the measured resonance frequency shifts downward because of the existence of the PLA mold. The measured -10dB fractional bandwidth are 2.2% and 1.3% respectively for antenna A and B, a typical characteristic of electrically small antennas.

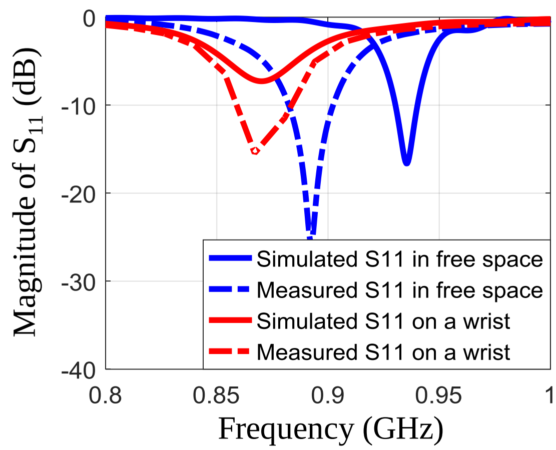

(a)

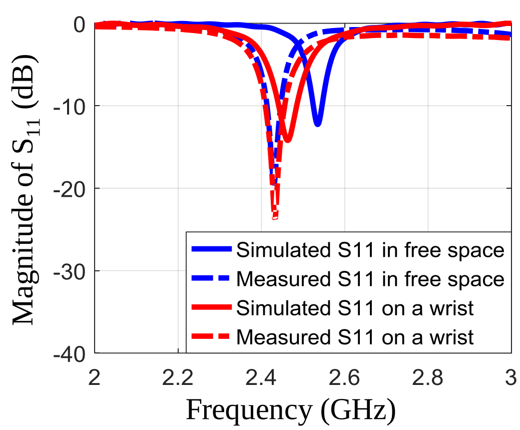

(b)

Fig. 2.2 Simulated and measured $|S_{11}|$ of (a) antenna A and (b) antenna B.

Next, we place the FCH antennas on the left wrist of a human subject and investigate the effect of the existence of the body on the resonance characteristic. Fig. 2.3 (a) shows the simulation model with the FCH antenna worn the left wrist of a voxel model

‘Gustav’ from CST, with voxel resolution of 2 mm. To save simulation time, only the left arm and hand are included in the simulation model. Fig. 2.3 (b) illustrates the reflection coefficient measurement setup on the left wrist of a male human subject. Both simulation and measurement results have been added in Fig. 2.2, as shown in red solid and red dashed curves. It is observed that the resonance frequencies of both FCH antennas shift slightly lower when the antenna is placed on the human wrist.

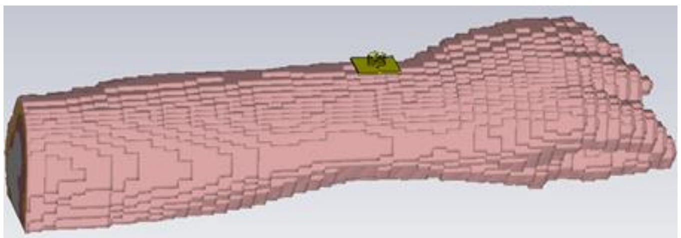

(a)

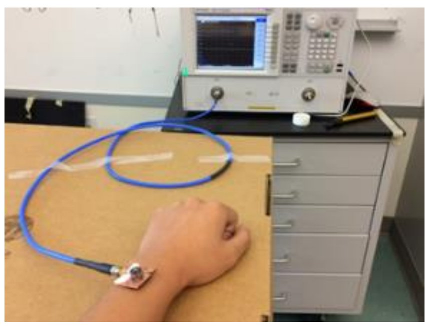

(b)

Fig. 2.3 (a) Simulation model, and (b) measurement setup for a wrist-worn FCH.

We also simulate the near electric field distributions of both wrist-worn FCH antennas at their resonance frequencies, as shown in Fig. 2.4 on a decibel scale. The field intensity of antenna A is much stronger than that of antenna B, since it operates at a much lower frequency. It is also shown that the electric field propagates along the surface of the hand towards the tip of fingers in both cases. As the fingers move, it is expected that near field perturbations of the antenna will cause its reflection coefficient to change, resulting in unique pattern of variations for classification purposes.

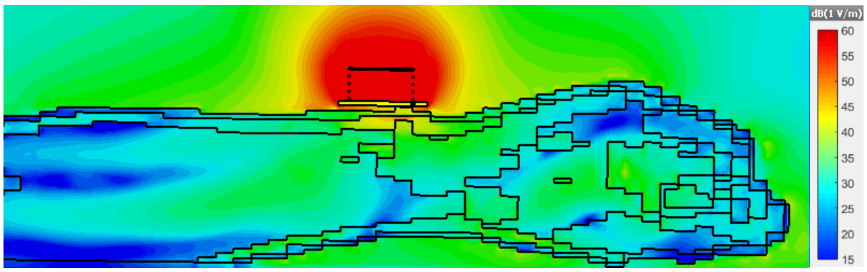

(a)

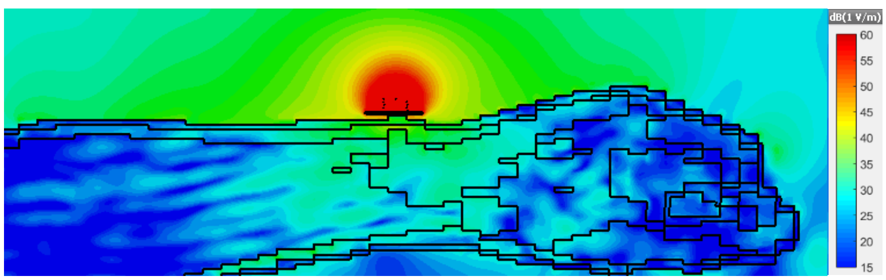

(b)

Fig. 2.4 Simulated electric field intensity distribution at the resonance frequency: (a) antenna A at 890 MHz; (b) antenna B at 2430 MHz.

2.2 Folded Cylindrical Helix Array

Since the radiation pattern of a single FCH antenna is isotropic in elevation plane, it is found that when the FCH is mounted on a human wrist, its input impedance is sensitive to not only finger motions, but also surrounding objects. So we proposed to design a FCH array in order to focus the antenna main beam in end-fire direction, so that it will not pick up as much the surrounding interference as a single FCH. In this dissertation, the FCH array is designed to be mounted on body chest to monitor the mouth and head activities. To design the FCH array, we need to investigate the phase delay between two adjacent FCH elements and optimize the array dimensions to achieve the optimum phase difference.

2.2.1 Wave Propagation along a 1-D FCH Array

First, a single 4-arm FCH element centered at 400 MHz is designed by using formulas provided in [62]. The helix radius R, height H, and number of turns are 0.0317 m, 0.047 m and 1, respectively. The height of the folded helix corresponds to 0.063 λ_o, which is much shorter than that of a quarter wavelength monopole antenna. Next, 21 identical elements are placed along a straight line in the y axis to form the FCH array. The inter-element spacing S is equal to 0.08 m, corresponding to 0.11 λ_o at 400MHz. Fig. 2.5 (a) and (b) show the simulation and measurement setup of the FCH array. While a finite sized metal ground plane is used in the measurement, an infinitely large perfect electric conductor (PEC) ground is assumed in the simulation to save computational time. A voltage source is placed at the bottom of the left-most element and a field probe is moved in between parasitic elements to sample the near electric fields at the ground plane level for different frequencies. Numerical software FEKO [63] is used for simulation and a vector network analyzer (Agilent PNL N5230C) is applied for measurement.

Fig. 2.6 compares the simulated and measured reflection coefficients S11 of the source antenna. They exhibit similar trend and both are significantly different from the sharp resonance behavior of a single FCH antenna, as presented in [62]. This is due to the strong coupling between closely-spaced helixes. The resonance band in the measurement shifts downward by approximately 20 MHz comparing to the simulation data, which can be attributed to manufacturing errors.

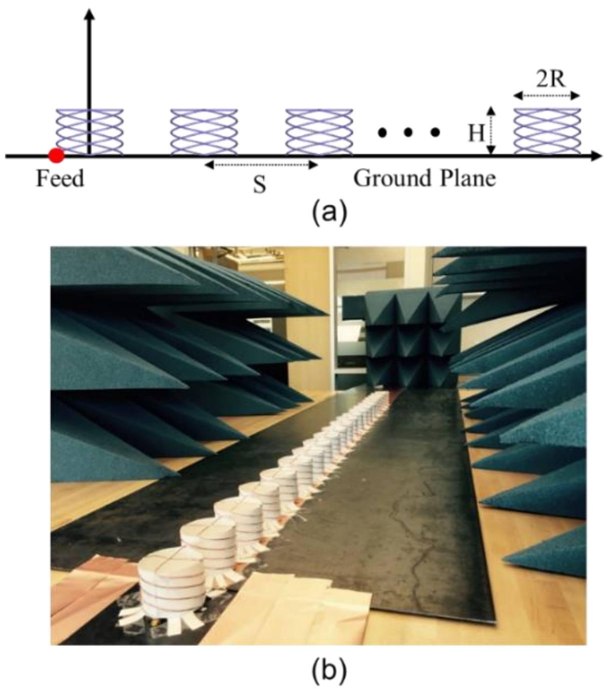

Fig. 2.5 1-D folded cylindrical helix array setup: (a) simulation (b) measurement.

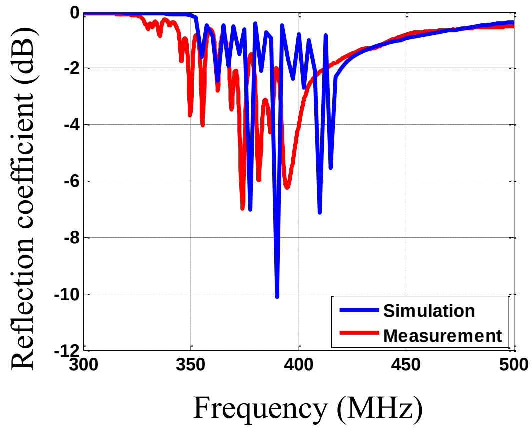

Fig. 2.6 Simulated and measured reflection coefficients.

Fig. 2.7 (a) and (b) show the normalized transmission data for both simulations and measurements on a dB scale. The antenna mismatches have been removed by normalizing $|S_{21}|^2$ to $1-|S_{11}|^2$ and $1-|S_{22}|^2$. The horizontal axis represents the frequency from 300 MHz to 500 MHz with an interval of 2.5 MHz, and the vertical axis represents the distance between transmitting and receiving antennas along the y axis from 0.4 m to 1.6 m with a spacing of 0.08 m. As shown in Fig. 2.7 (a), the receiving field strengths are much stronger between 355 MHz and 415 MHz, and within the pass band wave propagation exhibits negligible decay along the y axis. Outside of this pass band, field strengths are much weaker and attenuate much faster. The measurement results in Fig. 2.7 (b) show good agreement with simulation results, except the pass band shifts downward by approximately 20 MHz, similar to the above observation for Fig. 2.6.

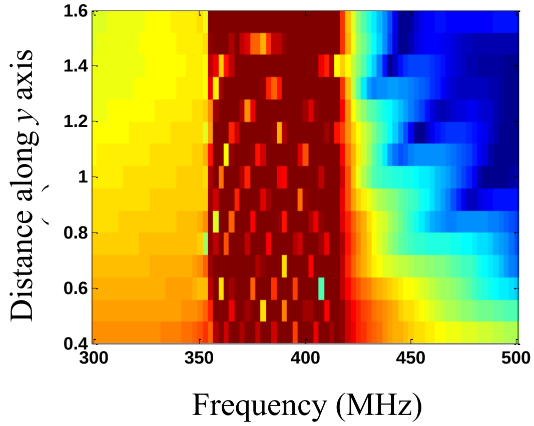

(a)

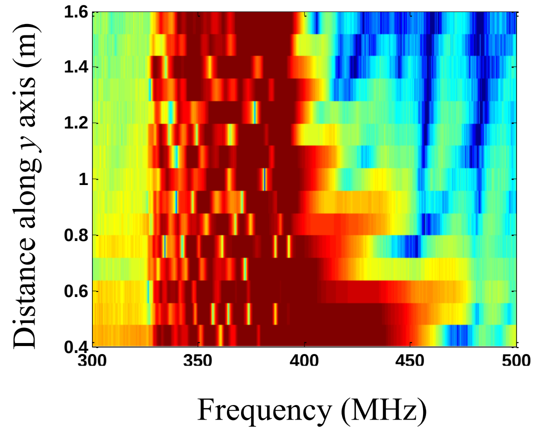

(b)

Fig. 2.7 Normalized transmission coefficients: (a) simulation, (b) measurement.

To further reveal the wave propagation along the FCH array, we simulate the near field distributions in the y-z plane at a sample frequency of 390 MHz. Fig. 2.8 plots the normalized near electric field components *Ey* and *Ez* on a dB scale. The horizontal axis represents the distance along the y axis from 0.4 to 1.6 m with a 0.08 m interval. The vertical axis represents height in the z direction from 0 to 0.2 m with an interval of 0.002 m. In Fig. 2.8 (a), a standing wave pattern can be clearly observed along the y direction, implying the interference between +*y* and -*y* traveling waves due to the finite size of the array. Along the z direction, the magnitude of *Ey* peaks at the height of the helix, and decays rapidly away from the interface between the FCH and the air. A similar interference pattern can be observed in Fig. 2.8 (b) for the *Ez* component, except its strength is much weaker than *Ey*.

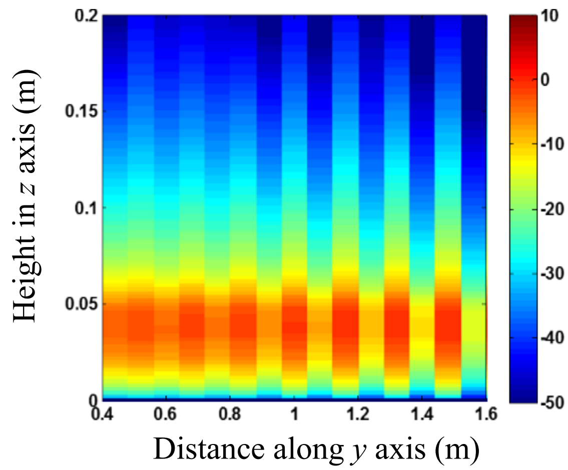

(a)

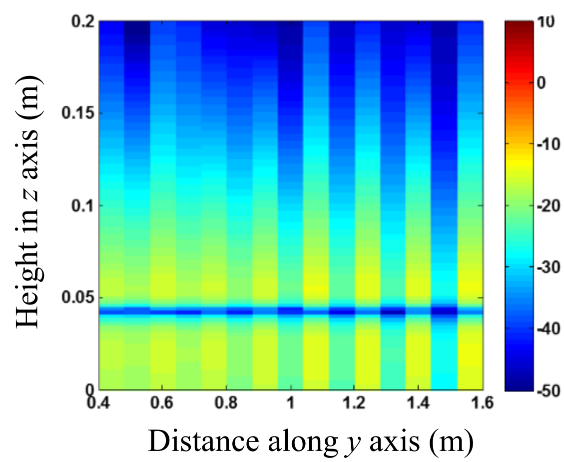

(b)

Fig. 2.8 Simulated near field distribution in the *y*-*z* plane at 390 MHz: (a) E_y (b) E_z

To better understand how wave propagates along the 1-D FCH array, we extract the dominant wave mode and its associated propagation characteristics from the above transmission and near field data. First we model the transmission data as a summation of different wave modes, each with a unique propagation constant β_m, attenuation constant α_m, and magnitude c_m, which can then be extracted using ESPRIT algorithm. ESPRIT is a super resolution spectrum estimation algorithm which was originally developed for estimation of sinusoid signals in noise [64]. More recently, it has been successfully applied to both wave propagation and antenna radiation problems [65]. The extraction process has been explained in detail in [66] and will not be repeated here.

$$S_{21} \cong \sum_{m=1}^{M} c_m e^{-j\beta_m y - \alpha_m y} \tag{1}$$

As an example, Fig. 2.9 (a) and (b) plot the ESPRIT fitted magnitude and phase curves at 390 MHz by adding the first two dominant terms. The results show excellent agreement with the original simulated transmission data, and the propagation constants of the two dominant terms are found to be -2.236k_o and 2.236k_o (k_o is the free space wave number), implying the superposition of incident and reflected components of a single slow wave mode. It is found that the dominant mode is a backward traveling surface wave for the following two reasons: first, the amplitude of the mode with a propagation constant $\beta = -2.236k_0$ is stronger than other modes extracted from the ESPRIT; second, the unwrapped phase increases as distance y increases, as shown in Fig. 2.9 (b), implying the dominant mode is a backward traveling wave. The ESPRIT algorithm is also applied to the measured transmission data at 370 MHz and the comparison between original and fitted data are shown in Fig. 2.9 (c) and (d). We intentionally shift the frequency downward by 20 MHz to make a fair comparison between simulation and measurement, as stated in above section. Table 3 shows the propagation constants of the dominant backward surface wave, and the results are very similar between simulation and measurement.

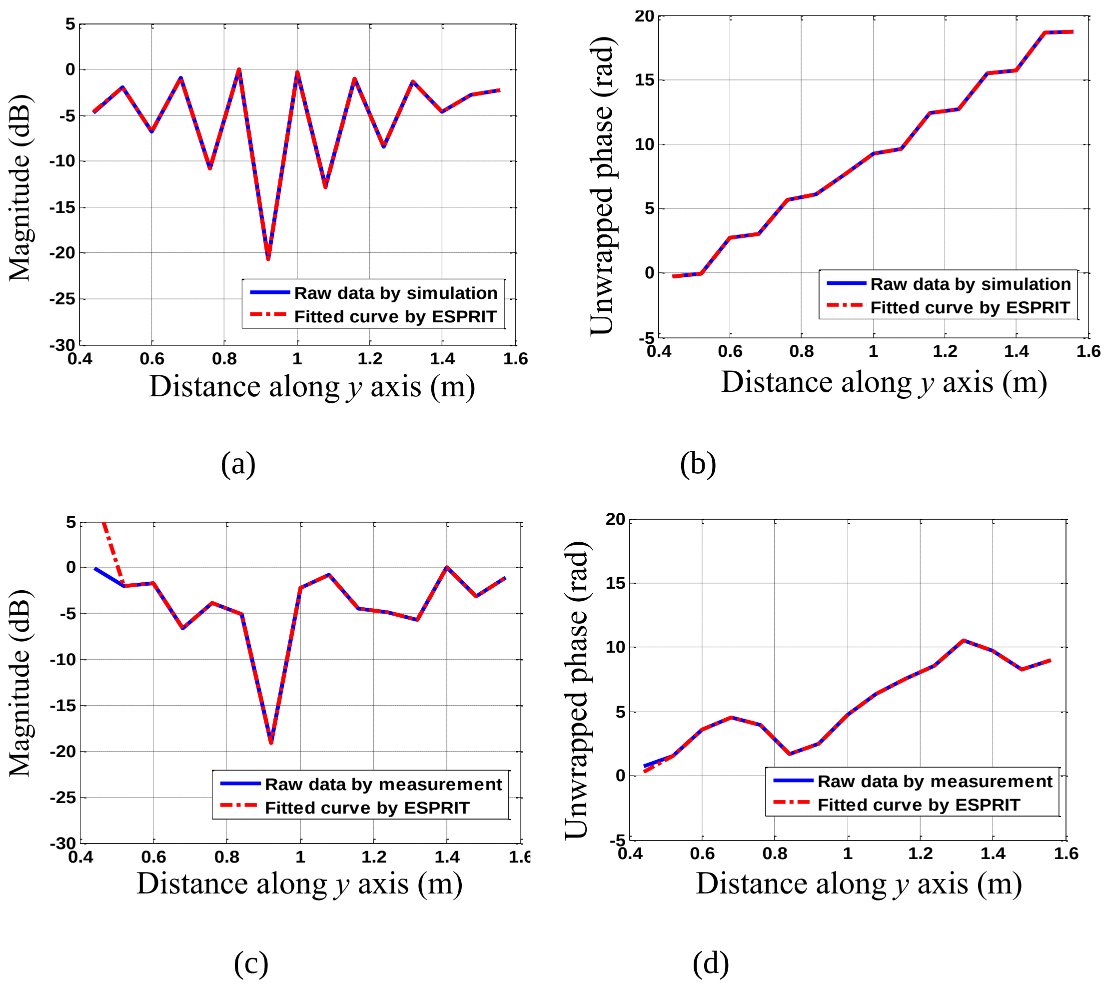

Fig. 2.9 Comparison between original data with fitted results by ESPRIT: (a) Simulated magnitude at 390 MHz (b) Simulated unwrapped phase at 390 MHz (c) Measured magnitude at 370 MHz (d) Measured unwrapped phase at 370 MHz

Table 3 Propagation parameters of the dominant mode

Dominant Mode	β_m/k_0	α_m/k_0
Simulation (390 MHz)	-2.236	0.0089
Measurement (370 MHz)	-2.4485	0.1584

Furthermore, we extract the mode distribution of the dominant surface wave from the simulated near electric field data in Fig. 2.10 (a) and (b). Fig. 2.10 (a) and (b) plot the extracted E_y and E_z mode distributions versus height z at 390 MHz. It can be seen that the magnitude of E_y peaks around the height of the FCH element (0.047 m) and decays exponentially away from the interface, a typical characteristic of surface wave propagation. The E_z distribution is more complicated below the interface between the FCH and the air, but is similar to E_y above the FCH height. We also map out the frequency dispersion behavior of the backward-traveling surface wave, and show the results in Fig. 2.11. It is seen that, except for the 20 MHz frequency shift along the horizontal axis, the values of β increase as frequency increases for both simulations and measurements.

Finally, a parametric study is conducted to correlate the propagation constant with array geometrical parameters. The first parameter we examined is the radius R. Both the height and spacing between elements are fixed. Fig. 2.12 (a) shows that β increases as R increases. The second varying parameter is the height H of the helix, as shown in Fig. 2.12 (b). The phase constant varies slightly since the total length of the helix does not change much. Finally, in Fig. 2.12 (c) we explored the effect of spacing and it was found that by increasing the interval of the adjacent element from 0.07 m to 0.1 m, the propagation constant drops from -1.83k_o to -2.49k_o due to the variation of coupling between array elements. It is concluded that by carefully selecting a combination of radius R, height H, and spacing S, we can achieve a desired propagation constant β for a fixed length FCH array. This observation is rather important for the surface wave antenna design, as will be explained in the next section.

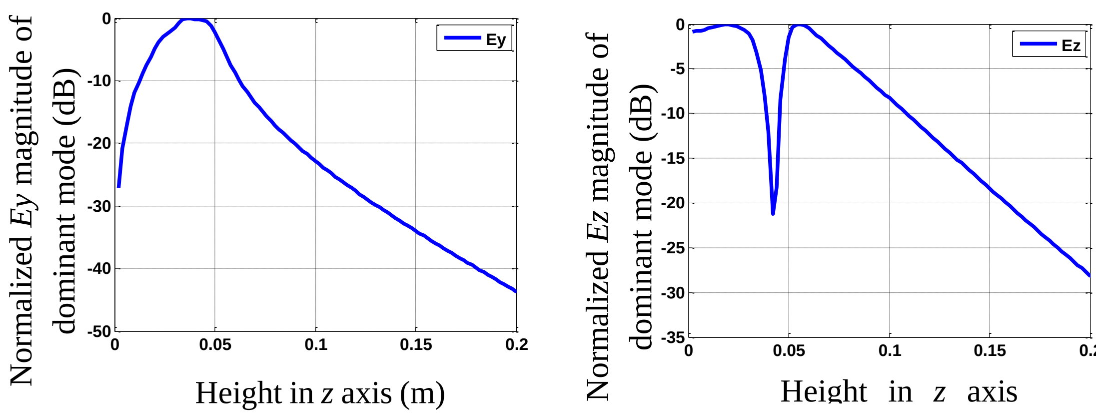

(a) (b)

Fig. 2.10 Normalized electric field mode distributions at 390 MHz: (a) *Ey* (b) *Ez.*

Finally, a parametric study is conducted to correlate the propagation constant with array geometrical parameters. The first parameter we examined is the radius R. Both the height and spacing between elements are fixed. Fig. 2.12 (a) shows that β increases as R increases. The second varying parameter is the height H of the helix, as shown in Fig. 2.12 (b). The phase constant varies slightly since the total length of the helix does not change much. Finally, in Fig. 2.12 (c) we explored the effect of spacing and it was found that by increasing the interval of the adjacent element from 0.07 m to 0.1 m, the propagation constant drops from -1.83k_o to -2.49k_o due to the variation of coupling between array elements. It is concluded that by carefully selecting a combination of radius R, height H, and spacing S, we can achieve a desired propagation constant β for a fixed length FCH array. This observation is rather important for the surface wave antenna design, as will be explained in the next section.

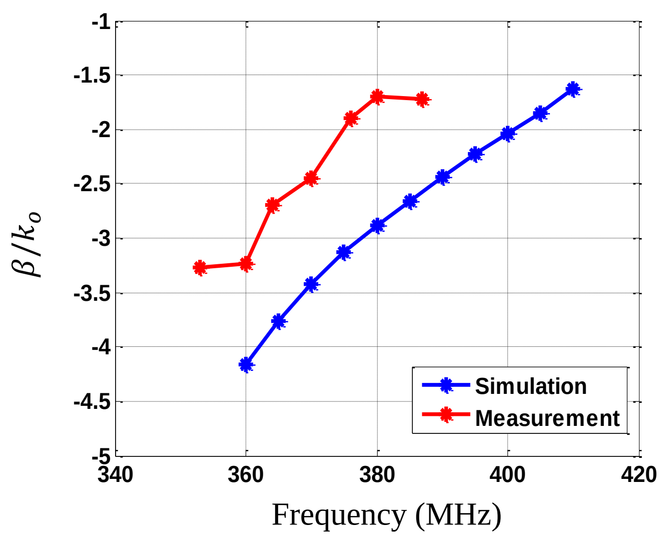

Fig. 2.11 Extracted phase constants of simulation and measurement against frequency.

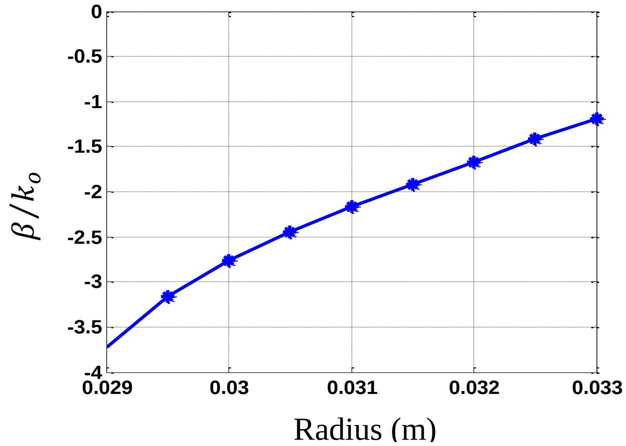

(a)

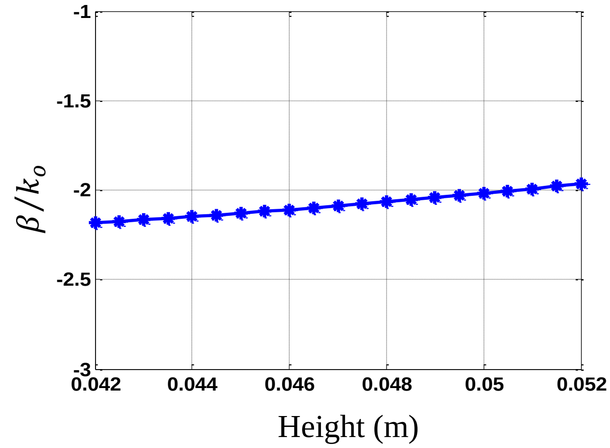

(b)

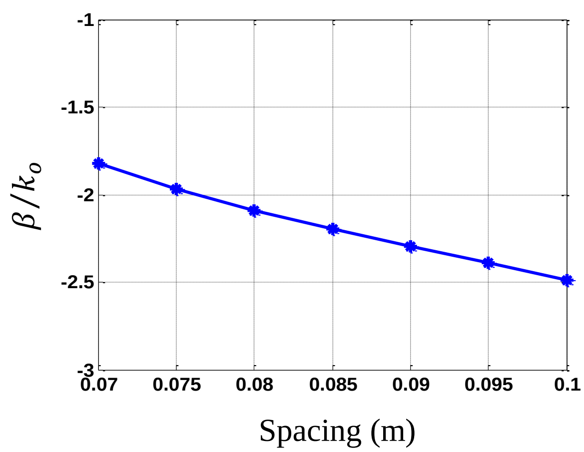

(c)

Fig. 2.12 Parametric study on array geometry: (a) radius (b) height (c) spacing.

2.2.2 Backfire FCH Array Design in Free Space

In this section, a compact 1-D, closely-spaced parasitic antenna array centered at 400 MHz is designed based on the above identified dominant surface wave mechanism. The total length of the array is assumed to be 0.5 λ_0. Given this fixed array size, the propagation constant of the surface wave has to be carefully determined to maximize the directivity of the array, which is similar to the 1-D metal wire antenna array design [66]. The optimum phase constant β_{opt} for this half wavelength array is found to be -1.98 k_0. Then the radius *R*, height *H*, and spacing *S* are selected to be 0.03115 m, 0.049 m and 0.104 m to achieve this β_{opt}. Other combinations of array geometrical parameters can also result in this optimum propagation constant, as discussed in the previous parametric study. Fig. 2.13 plots the final array design setup, which consists of four FCH elements. The height of the source antenna is tuned to be 0.042 m to match the input impedance to 50 Ohm at the center frequency.

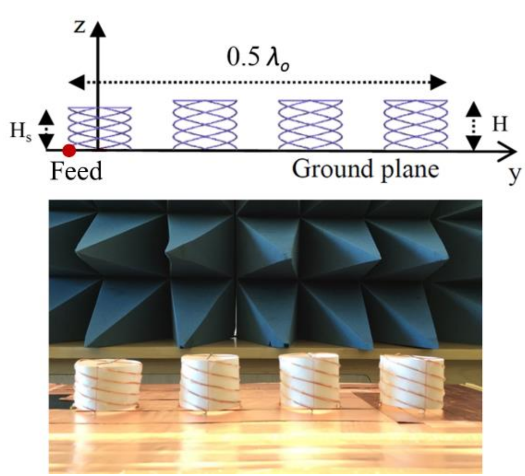

Fig. 2.13 1-D compact, closely-spaced backfire antenna array.

Fig. 2.14 shows the antenna reflection coefficients versus frequency. The center resonance frequencies are found to be 400 MHz and 386 MHz for simulation and measurement. Both of the -10dB bandwidthes are 3 MHz. Fig. 2.15 compares the simulated and measured gain in the backward endfire direction (θ=90°, ϕ=270°). The maximum gain values are 10.99 dBi for simulation and 10.33 dBi for measurement. Finally, Fig. 2.16 plots the simulated antenna array radiation patterns in both the azimuth plane (i.e., xy plane) and elevation plane (i.e., yz plane) at the center frequency, which clearly shows the backward radiation pattern. The simulated front-to-back ratio is found to be 9.4 dB, while in measurement it is 12.8 dB.

To provide more physical insights into our FCH array operation, we compare its inter-element phase delay with the well-known Hansen-Woodyard endfire array condition [13]. Given the extracted propagation constant (-1.98 k_0) and spacing (0.138 λ_0), the phase delay θ_0 between adjacent FCH elements is found to be:

$$\theta_0 = \beta_{opt} d = -1.98 k_0 \times 0.138 \lambda_0 = -1.72\, rad \tag{2}$$

According to the Hansen-Woodyard endfire array condition, the theoretical optimum phase delay θ_{HW} between adjacent array elements should be close to:

$$\theta_{HW} = -\left(k_0 d + \frac{\pi}{N}\right) = -\left(\frac{2\pi f d}{c} + \frac{\pi}{N}\right) = -1.6525\, rad \tag{3}$$

where c is speed of light, and N is number of elements. It can be seen that the phase delay of our FCH array θ_0 is close to that of Hansen-Woodyard endfire condition θ_{HW}, resulting in its maximum radiation in the $-y$ direction.

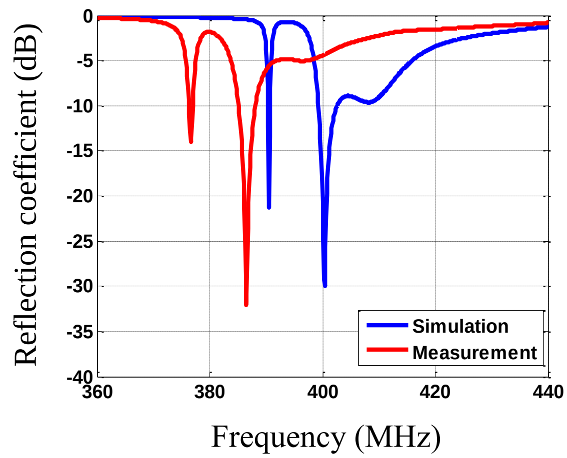

Fig. 2.14 Simulated and measured antenna reflection coefficients.

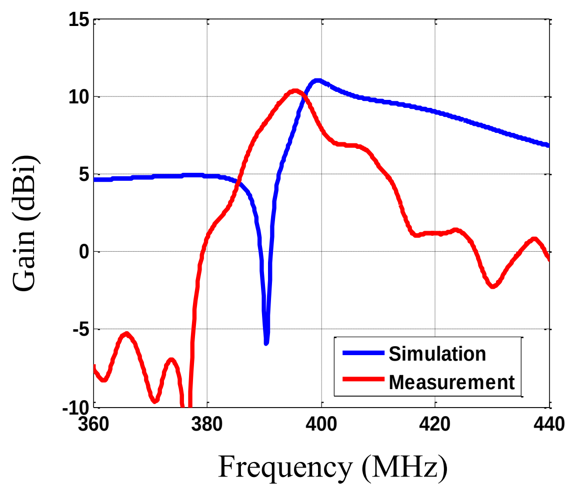

Fig. 2.15 Simulated and measured antenna gain.

Finally, we compare our FCH antenna array performance with other small antenna arrays in literatures [67-70]. The comparison is shown in Table 4 below. It can be clearly seen that our FCH array exhibits the lowest height, highest gain and best front to back (F/B) ratio among all antennas. The trade-offs we made include one more element and slightly larger spacing. The -10 dB input bandwidth of our antenna is the smallest, which can be attributed to the lowest height of the FCH element.

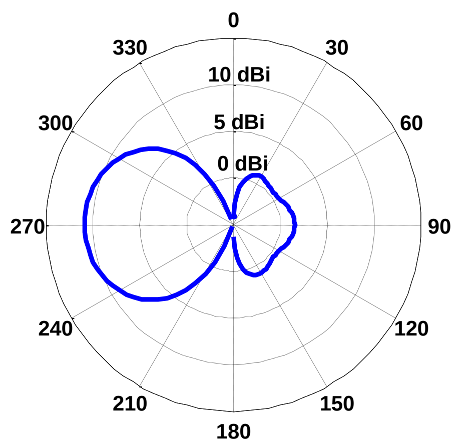

(a)

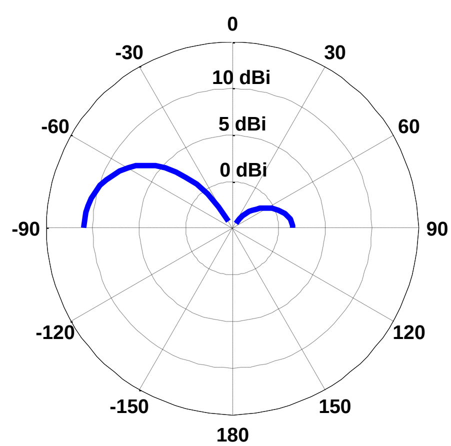

(b)

Fig. 2.16 Simulated radiation patterns: (a) Azimuth plane (b) Elevation plane.

Table 4 Comparison between our antenna and other small antenna arrays in literatures.

Antenna	Elements	Spacing	Height	Gain	F/B	BW
Our Antenna	4	$0.138\lambda_0$	$0.06\lambda_0$	10.3 dBi	12.8 dB	0.75%
Ref. [67]	3	$0.11\lambda_0$	$0.275\lambda_0$	7.14 dBi	8.6 dB	2.28%
Ref. [68]	3	$0.06\lambda_0$	$0.092\lambda_0$	8.5 dBi	7 dB	2.7%
Ref. [69]	3	$0.09\lambda_0$	$0.1\lambda_0$	8.43 dBi	6.63 dB	1.2%
Ref. [70]	3	$0.053\lambda_0$	$0.21\lambda_0$	9.9 dBi	n/a	12.44%

2.2.3 Wearable FCH Array

After designing the FCH array in free space, we proposed to use this antenna on human body. We redesigned the FCH array at 2.4 GHz, so its size can be much smaller than the 400 MHz antenna we designed above. Fig. 2.17 shows the designed FCH at 2.4 GHz and Table 5 gives the dimension of the FCH structure. The first element of the FCH array is a little smaller than the other three elements for impedance matching purpose, and it is represented as FCH1 in Table 5. The other 3 elements are represented by FCH2 in the table. Fig. 2.18 shows the fabricated FCH array working at 2.45 GHz. The ground plane has a size of 30 mm by 80 mm. The copper wire has a radius of 0.16 mm. The spacing between adjacent elements is 17 mm.

Table 5 FCH Dimensions.

Antenna	R (mm)	H (mm)	H1 (mm)
FCH1	4.87	6.8	1
FCH2	4.86	5.64	0.83

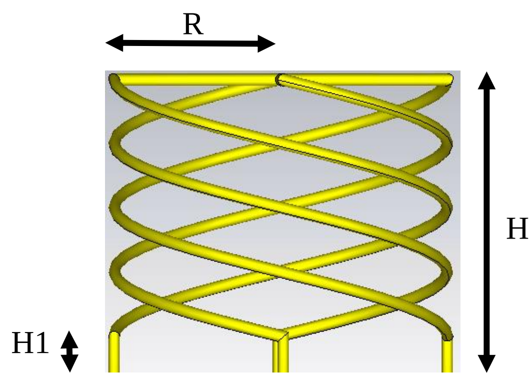

Fig. 2.17 FCH resonating around 2.45 GHz.

To investigate the antenna performance in vicinity with human body, we simulated the antenna on a human voxel model in CST [71]. Different locations was tried. As shown in Fig. 2. 19, the antenna was placed on the wrist and chest, with maximum radiation direction pointing toward fingers and head. Fig. 2.20 shows the antenna measurement setup. The antenna was placed on the same location as the simulation setup.

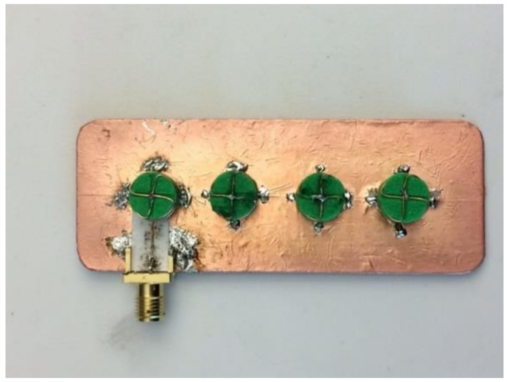

(a)

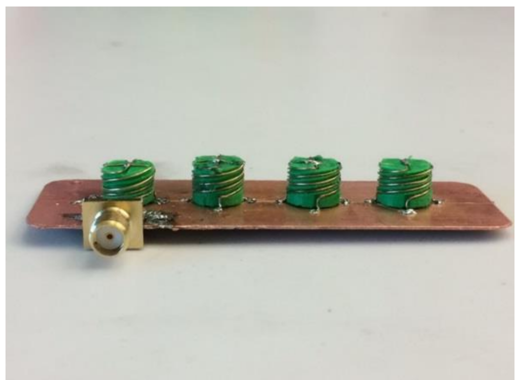

(b)

Fig. 2.18 Fabricated FCH array working at 2.45 GHz: (a) top view, (b) side view.

Fig. 2.21 shows a comparison of the simulated and measured reflection coefficients of the antenna both in open space, on human wrist and chest. The measurement results agree well with the simulation data. The resonance frequency is at 2.45 GHz. It is found that the resonance frequency does not change when the antenna is placed on human body, which indicates that human body doesn’t degrade the antenna performance. This is because the existence of ground plane isolate the antenna from human tissues. The antenna reflection coefficients when placed on wrist and chest are similar.

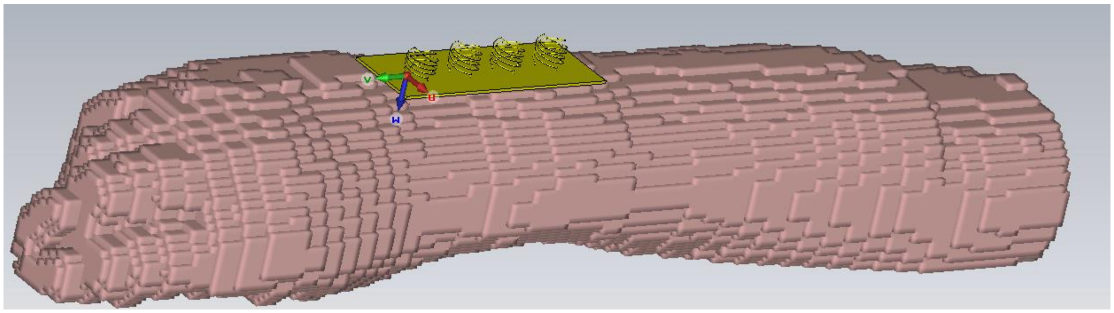

(a)

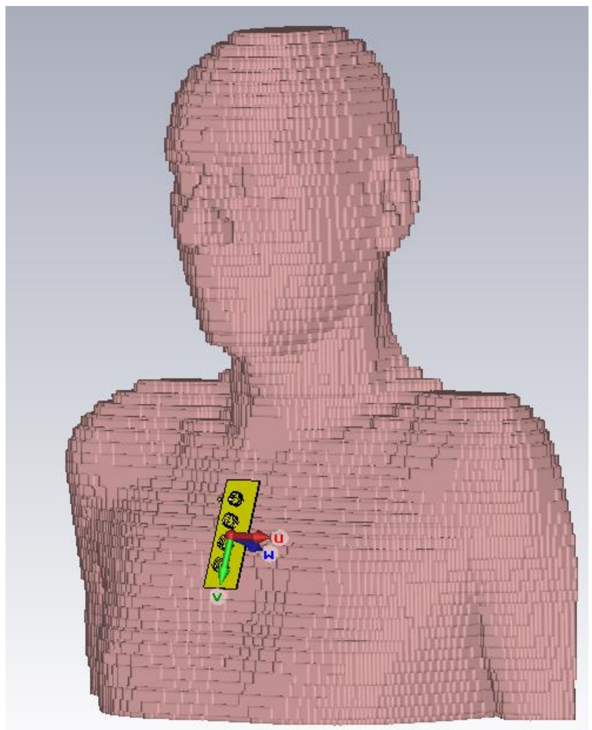

(b)

Fig. 2.19 Antenna simulation on human body (a) wrist, (b) chest.

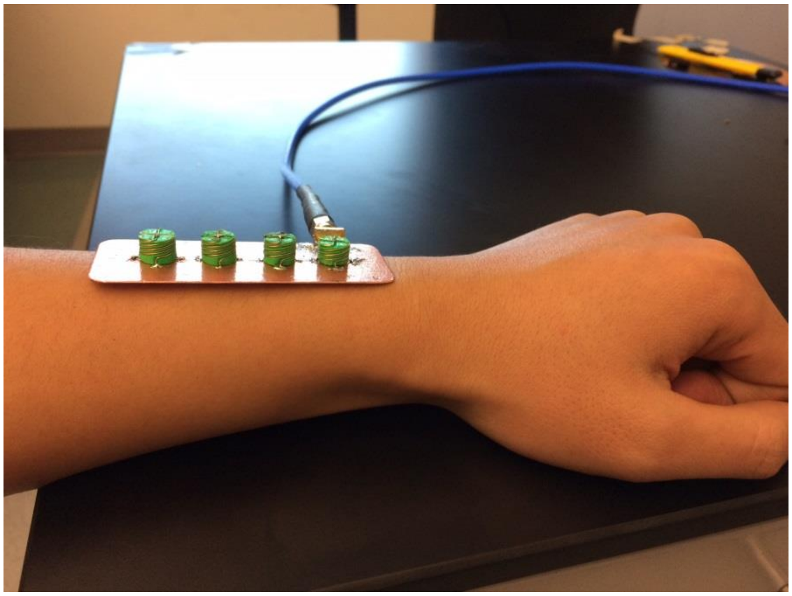

(a)

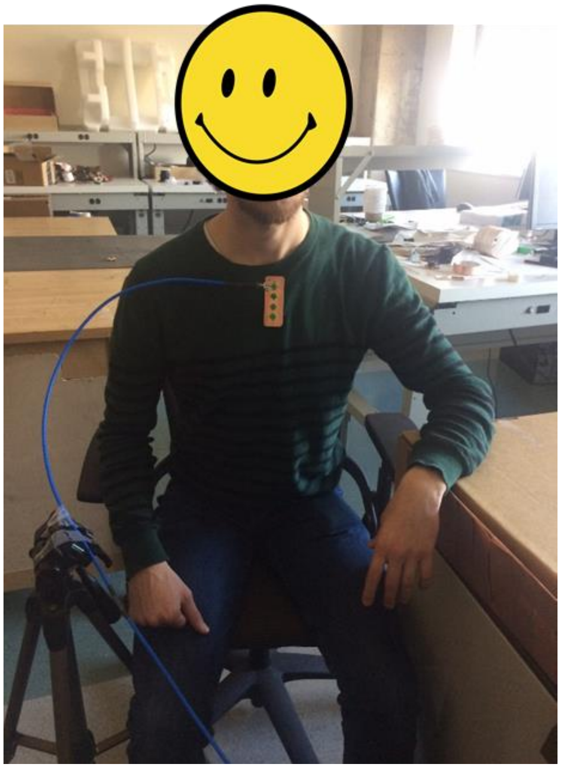

(b)

Fig. 2.20 Antenna measurement on body: (a) wrist, (b) chest.

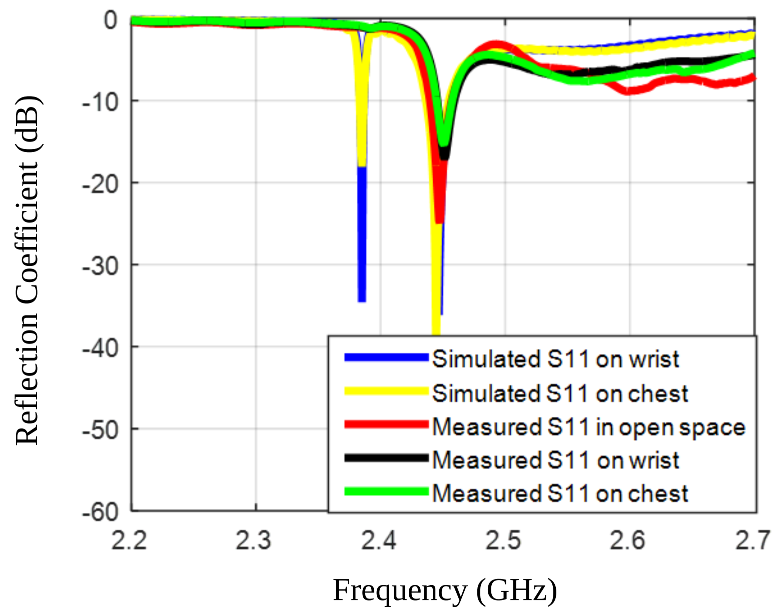

Fig. 2.21 Reflection coefficients of the wearable FCH array.

Fig. 2.22 plots the simulated 3D radiation pattern on wrist and chest. The antenna can achieve 6.25 dBi gain when placed on wrist, while it is only 2.49 dBi when placed on chest. This is because the torso has a larger area than the wrist. Thus, more electrical power is dissipated in torso tissues than wrist tissues. In other words, the efficiency of antenna on the chest is smaller than that on the wrist.

Fig. 2.23 plots the simulated and measured antenna gain against frequency. The antenna gain peaks around 2.45 GHz. The red line represent measured antenna gain on wrist. It is 1 dB lower than simulated gain on wrist. When the antenna is mounted on chest, head will block the maximum radiation direction so that it is hard to measure its gain on chest. Table 6 gives the simulated and measured front to back ratio of this antenna. In simulation, it can achieve 8.6 dB front to back ratio when placed on wrist, and 7.63 dB on chest. The measured data is slightly higher than simulation.

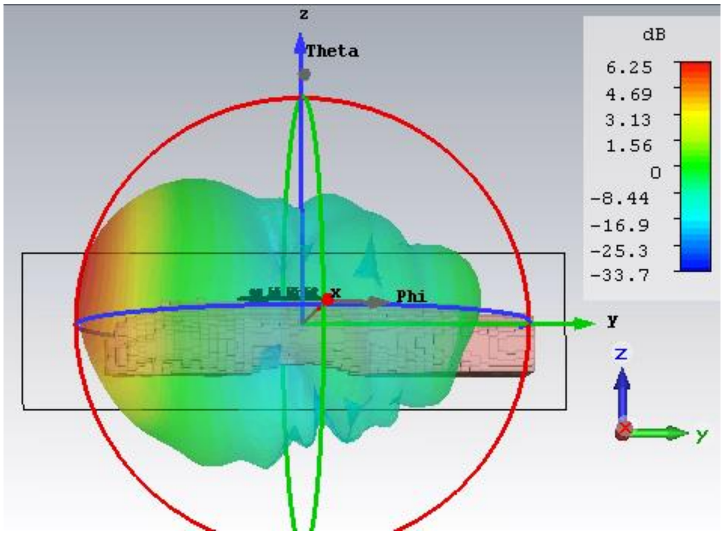

(a)

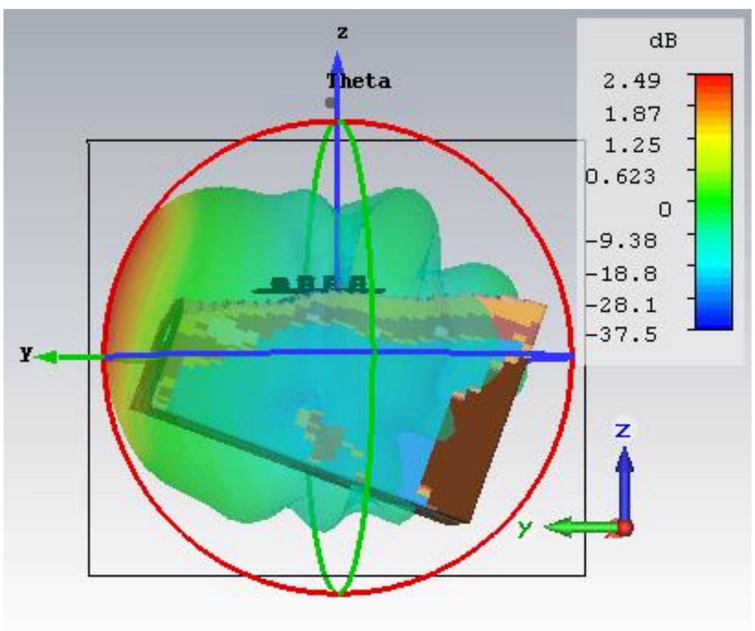

(b)

Fig. 2.22 Simulated 3D radiation pattern on (a) wrist, (b) chest.

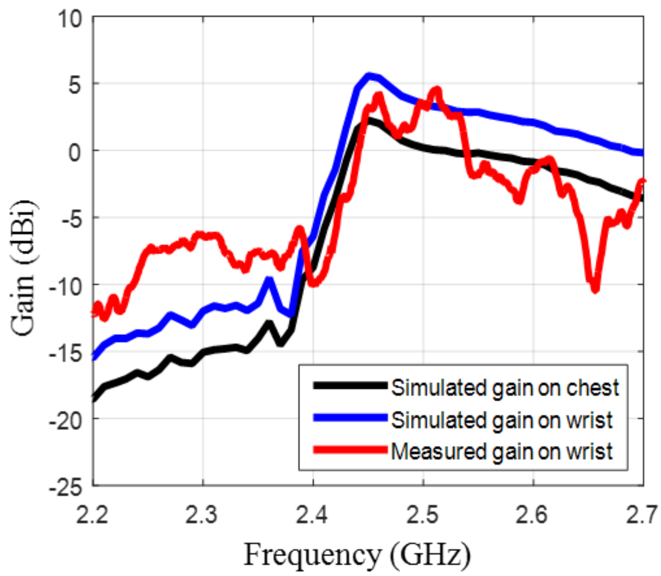

Fig. 2.23 Simulated and measured antenna gain against frequency.

Table 6 Front to back ratio

Body Position	On Wrist	On Chest
Simulation	8.64 dB	7.63 dB
Measurement	10.99 dB	7.7 dB

2.3 Summary

In this chapter, design and test result for a wearable 3D printed FCH antenna on human body have been presented. Then, the surface wave propagation and radiation along a 1-D FCH array have been investigated from both simulation and measurement perspectives. It is found that a backward traveling surface wave can be supported by this structure. The propagation characteristics of this dominant wave mechanism are extracted and discussed. Furthermore, a backfire surface wave antenna is designed and implemented based on the identified wave mechanism.

CHAPTER THREE

Wearable Textile Microstrip Antenna Design and Durability Tests

To integrate the wearable antenna more easily with clothing, we investigated the textile antenna and its performance variations under different harsh environments or wear conditions.

3.1 Durability Test on Conductive Textile Surface Resistivity

Wireless body area networks (WBAN) have been a trending topic in recent years because of their important applications in military, sports and wellness industries. Wearables, such as medical devices and popular monitoring devices such as smart watches and fitness trackers are being attached to the body, but because of several technical challenges they have not yet been fully integrated into the clothing. Electronic textile (E-textile) antennas and circuits show great potential to implement WBANs due to their low mass, physical flexibility and ease of integration with garments.

Many techniques and materials have been attempted to realize e-textiles. One common approach is the embroidery of metal-coated conductive threads on ordinary textiles/fabrics [72]. However, some of the metal-coated conductive threads are simply too fragile (leading to thread breakage) for use in standard embroidery machines. E-textiles can also be constructed by depositing a conductive metal layer on top of a fabric by conductive ink printing [73] or metal coating [74]. These approaches can provide excellent isotropic conductivity, and the end result has a much thinner profile compared to the embroidered option.

In order to integrate e-textiles into clothes, it is necessary to understand how environmental changes or wear conditions affect the e-textile performance. In [75], it was found that increasing the relative humidity of a textile antenna could increase the permittivity and loss tangent of the material. The antenna bending effect has also been studied [76, 77]. It was found that antenna bending could broaden the radiation pattern in the bending plane and change the impedance matching. In [78], the wearable antenna performance was tested in freezing environment. In spite of previous studies on the effect of environmental effect on textile antenna performance, more environmental or wear conditions needs to be considered.

Two types of e-textiles were identified and selected for this study. One is a nickel-copper-coated nylon ripstop (NC) (Fig. 3.1 (a)). The other e-textile is a jersey knit fabric with silver-coated cotton/polyester yarns (SJ) (Fig. 3.1 (b)). To illustrate the structure of these 2 fabrics, their microscope images are shown in Fig. 3.1 (c) and (d).

Surface resistivity tests were conducted according to AATCC test method 76 [79]. Fabric specimens were cut into 51x51 mm squares. Two copper electrodes were placed on opposite edges of the specimen, and the resistivity was measured by using a Fluke 298 multimeter with an accuracy of 0.02 Ohm. The surface resistivity was measured in both warp (wales) and filling (course) yarn directions of the e-textile. Table 7 shows results of surface resistivity measures of the two fabrics. The resistivity of NC in filling yarn direction is similar with that in warp direction. Due to the loop structure of the weft knit fabric, the SJ resistivity in the wale direction is much larger than that in the course direction. Overall, the NC fabric has better conductivity than SJ fabric.

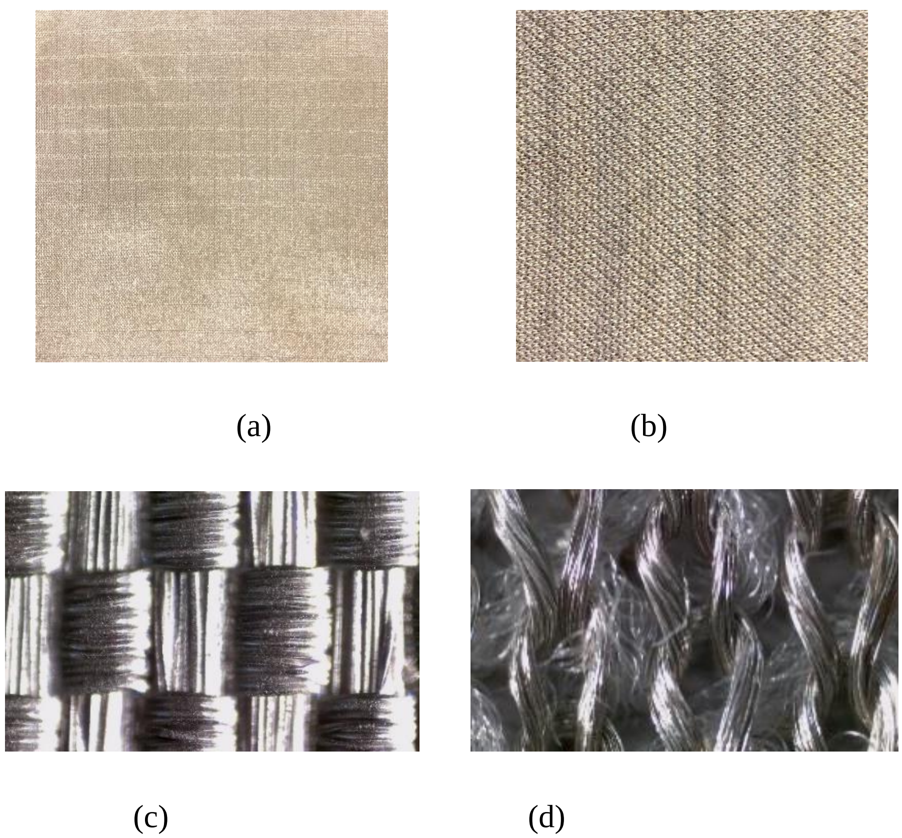

Fig. 3.1 Photos of the two e-textiles (a) nickel-copper ripstop (NC) (b) silver jersey (SJ) (c) NC microscope image (d) SJ microscope image.

Table 7 The surface resistivity of NC and SJ fabrics before treatment.

Fabric Resistivity (Ohm/Square)	NC	SJ
Filling/Course	0.03	1.28
Warp/Wales	0.04	2.35

Fabrics were subjected to moisture, perspiration, laundering, abrasion, pilling, and wrinkling tests, which are all based on AATCC/ASTM standards as shown in Table 8 [79, 84]. For purposes of measuring resistivity, some modifications to procedures were necessary as indicated in the description column of Table 8. For each treatment, three specimens were tested for resistivity and average data is presented.

3.1.1 Moisture

The surface resistivity of specimens was measured immediately after 10 minutes of submersion in water and again after air-drying. Fig. 3.2 (a) and (b) illustrate the effect of moisture on the surface resistivity of the two fabrics. Moisture did not change the NC resistivity, but a decrease was observed in the SJ wales direction. After air-drying, the resistivity of both fabrics returned to their original values.

Table 8 Durability test methods

ASTM/AATCC Test Method	Effect on Resistivity	Description/Modifications
NA	Moisture	Specimens were soaked in distilled water for 10 minutes with occasional agitation.
AATCC TM15: Colorfastness to Perspiration	Perspiration	Test procedure was followed, but without multifiber strips. Specimen size was reduced from 64 mm to 51mm square.
AATCC TM61: Colorfastness to Laundering, accelerated	Laundering	Specimen size was reduced from 51 x 152 mm to 76 mm square. Followed Test Condition No. 1B with 1mL additive per canister.
ASTM D3884: Abrasion Resistance (Rotary Platform, Double Head Method)	Abrasion	A 1000g load and H-18 wheels were used, selected based on the test method's recommendations for coated metal textiles.
ASTM D3512: Pilling Resistance (Random Tumble Pilling Method)	Pilling	114 mm square bias-cut specimens were treated with Fray Check. After testing, specimens were trimmed down to 51 x 51 mm squares, no longer on bias.
AATCC TM128: Wrinkle Recovery (Appearance Method)	Wrinkle	152 x 279 mm specimens were wrinkled under pressure until reaching an appearance rating of 1, then trimmed to 51 mm squares.

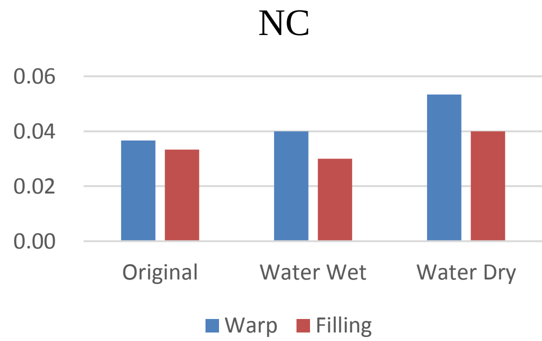

(a)

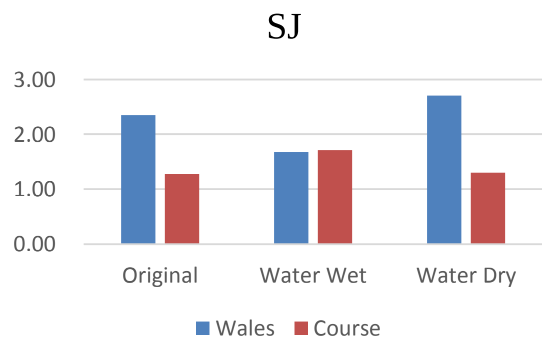

(b)

Fig. 3.2 The moisture effect on surface resistivity of (a) NC and (b) SJ.

3.1.2 Perspiration

Effects of perspiration were tested using AATCC TM15. This test is designed to assess colorfastness to perspiration, but we instead measured the change in surface resistivity. In the photos of fabrics after perspiration tests (Fig. 3.3), chemical residues can be clearly observed on both specimens. Fig.3.4 shows resistivity changes after the perspiration test. The resistivity of NC increased, possibly due to the presence of the observed residue. The resistivity of SJ in the wales direction decreased, thus the perspiration solution appears to assist conductivity in that yarn direction.

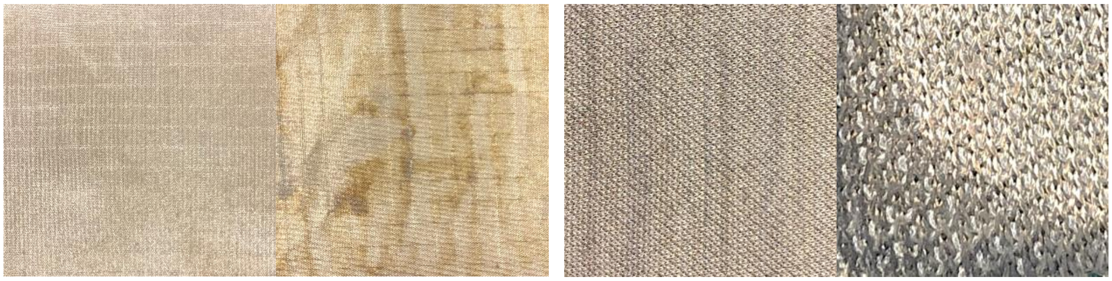

(a1) (a2) (b1) (b2)

Fig. 3.3 Photos of NC (a1) pre- and (a2) post-perspiration test and SJ (b1) pre- and (b2) post-perspiration test.

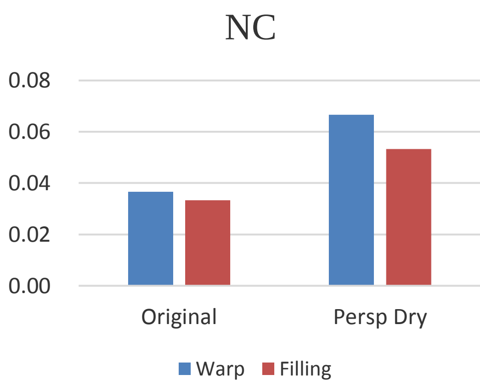

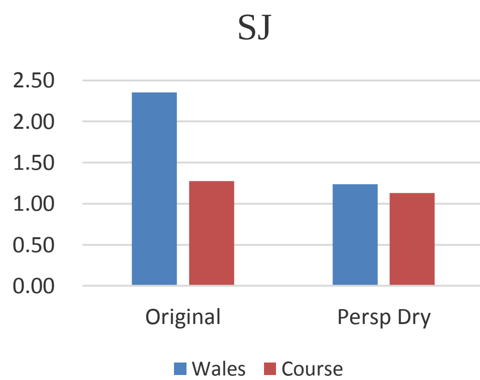

(a) (b)

Fig. 3.4 The effect of perspiration on surface resistivity of (a) NC and (b) SJ.

3.1.3 Laundering

Laundering studies were based on AATCC TM 61: Test Condition No. 1B, which simulates five home launderings in only 20 minutes. This method is designed to test colorfastness to laundering, but we instead measured changes in surface resistivity. AATCC TM61 allowed us to test small specimens, against a variety of home laundering products, under standard and controlled conditions. Each Rotowash canister contained 10 rubber balls, one e-textile specimen, and a solution of 150mL distilled water and 1mL additive. Additives included:

- AATCC Standard Reference High Efficiency Detergent
- Seventh Generation Free & Clear Plant-Based Detergent
- Texcare Detergent (a factory recommended detergent for e-textiles)
- Downy Free & Clear Fabric Softener

After laundering, specimens were trimmed to 51 mm square, rinsed with distilled water, and air-dried.

The surface resistivity of NC slightly increased, particularly for standard detergent and softener, as shown in Fig. 3.5 (a). This may have resulted from a chemical reaction between the detergent and the e-textile, or due to loss of metal coating. The surface resistivity of SJ fabric in the wales direction decreased (Fig. 3.5(b)), which may be due to observed shrinkage in that direction. Laundering did not affect the SJ resistivity in the course direction.

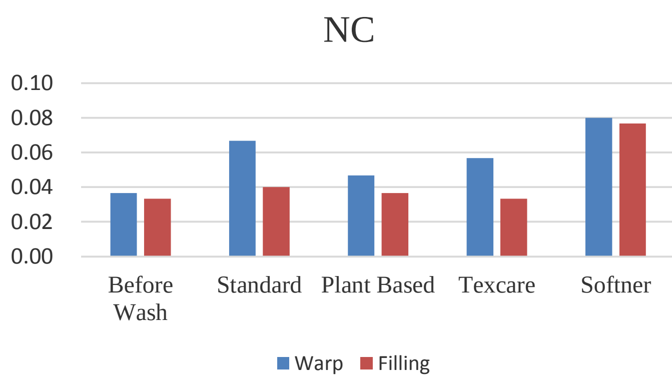

(a)

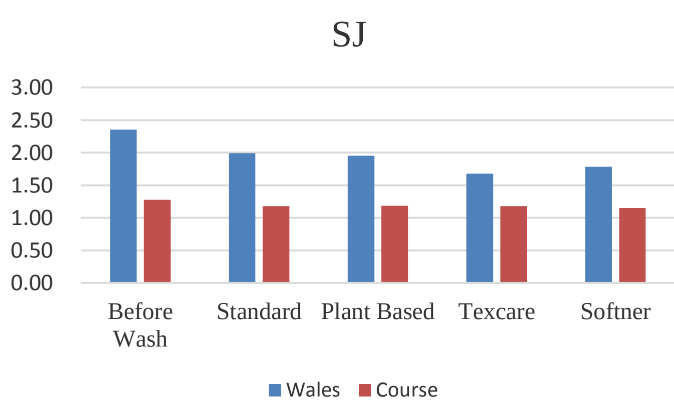

(b)

Fig. 3.5 Laundry effect on surface resistivity of (a) NC and (b) SJ.

3.1.4 Taber Abrasion

Abrasion tests were conducted following ASTM D3884. To explore resistivity changes after varying degrees of abrasion, specimens were subjected to 20 and 40 abrasive revolutions. As evident in Fig. 3.6, 40 cycles caused considerably more damage to the fabric than 20 cycles. Fig. 3.7 illustrates resistivity changes after the abrasion test. The surface resistivity of NC increased as the number of abrasive revolutions increased. Conversely, SJ resistivity in the wales direction decreased after abrasion.

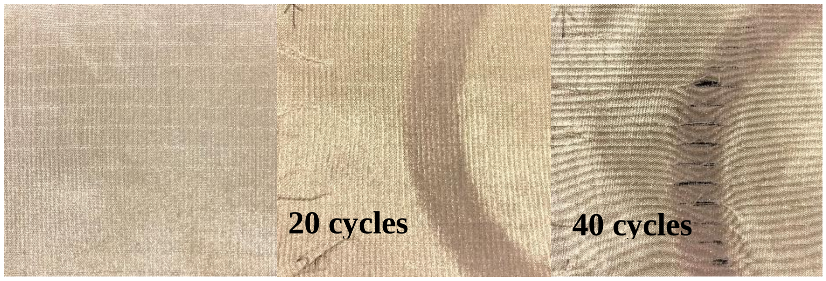

(a)

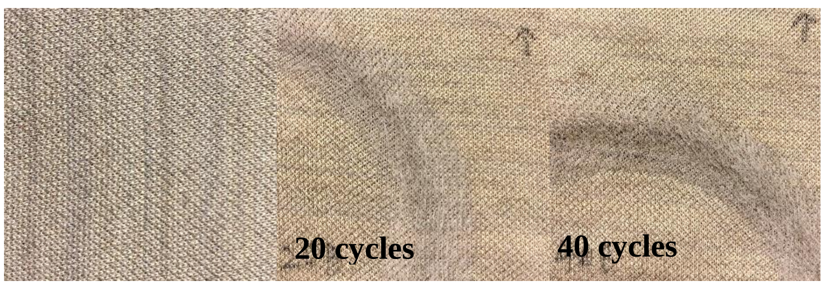

(b)

Fig. 3.6 Photos of (a) NC and (b) SJ after abrasion test.

3.1.5 Pilling

The surfaces of e-textile specimens were pilled in a Random Tumble Pilling Tester following ASTM D3512. After 30 minutes of tumbling, NC showed no visible pilling - a rating of 5 on the Photographic Standards for Random Tumble Pilling Test. However, it did curl significantly (as shown in Fig. 3.8 (a2)), showed severe damage to the textile, and became completely non-conductive. The SJ fabric did not curl and pilled to a rating of 4 (as shown in Fig. 3.8 (b2). Its surface resistivities increased by 1.7 and 0.7 Ohm/sq respectively in wales and course direction (Fig. 3.9).

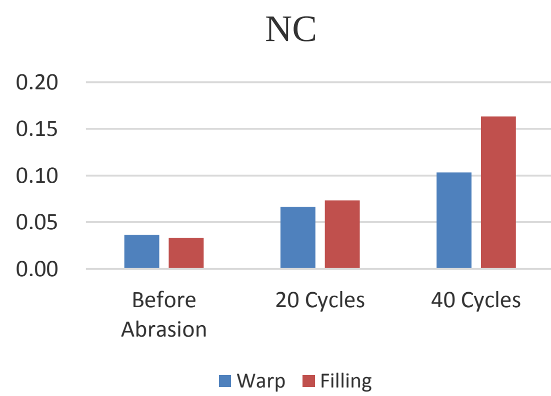

(a)

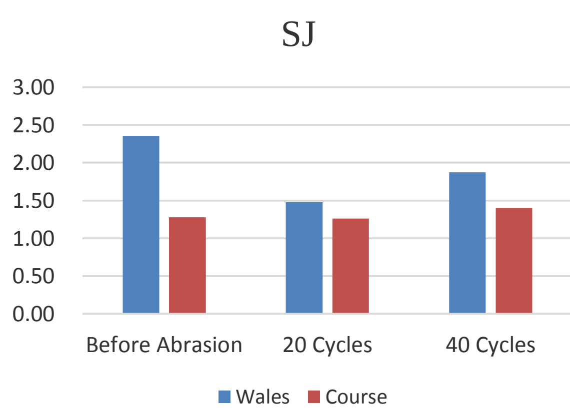

(b)

Fig. 3.7 Abrasion effect on surface resistivity of (a) NC and (b) SJ.

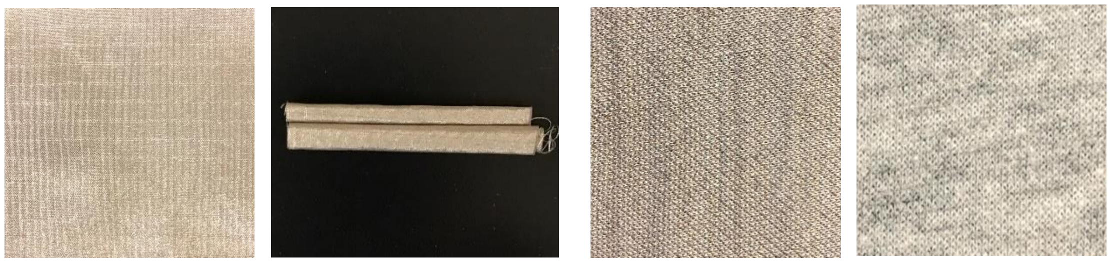

(a1) (a2) (b1) (b2)

Fig. 3.8 Photos of NC (a1) pre- and (a2) post-pilling test and SJ (b1) pre and (b2) post-pilling test.

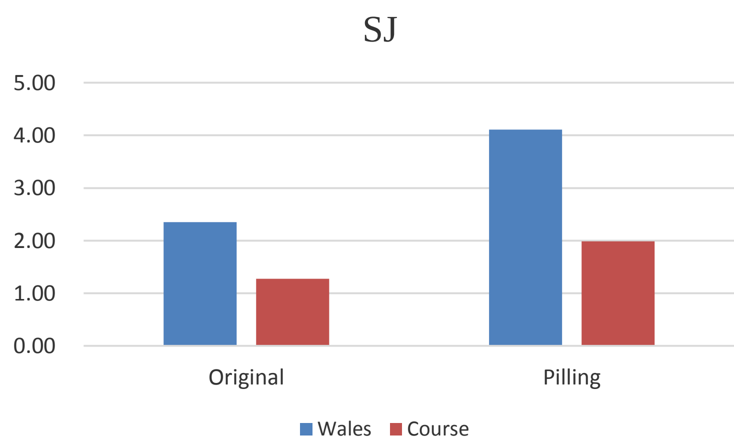

Fig. 3.9 The surface resistivity of SJ before and after pilling test.

3.1.6 Wrinkling

Wrinkles were induced in e-textile specimens as outlined in AATCC TM128. Specimens remained in the AATCC Wrinkle Tester under a 3500g load until reaching a rating of 1 (as shown Fig 3.10 (a2) and (b2)) as indicated by the AATCC 3-Dimensional Wrinkle Recovery Replicas. Results suggest that wrinkling slightly increases the surface resistivity of e-textiles. NC had an increase of 0.05 and 0.03 Ohms/sq in the warp and filling direction (Fig. 3.11 (a)) and SJ had an increase of 0.07 and 0.46 Ohm/sq in the wales and course direction (Fig. 3.11 (b)).

(a1) (a2) (b1) (b2)

Fig. 3.10 Photos of NC (a1) pre- and (a2) post-wrinkling test and SJ (b1) pre and (b2) post-wrinkling test.

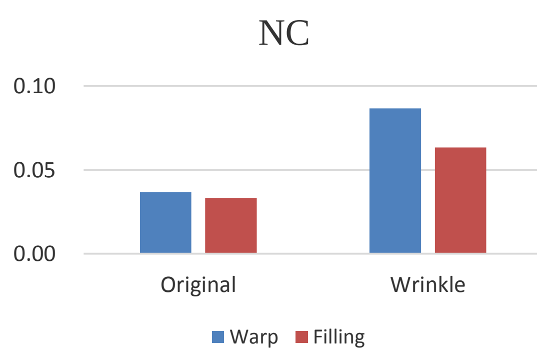

(a)

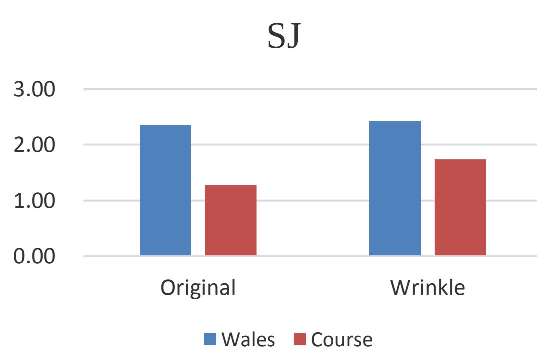

(b)

Fig. 3.11 The surface resistivity of (a) NC and (b) SJ before and after wrinkle test.

3.2 Textile Microstip Antenna Design

The surface resistivity study above was conducted at direct current (DC) frequency. As there is a gap in literature regarding the use of e-textiles for radio frequency (RF), the RF performance of e-textiles under harsh conditions also need to be investigated. A textile antenna was designed and its performance was examined under harsh conditions following the e-textile resistivity testing structure previously outlined. The textile antenna was designed from the NC fabric as the patch material, as its resistivity is much lower than SJ and more isotropic in different directions than SJ. Medium weight denim fabric (100% cotton) was selected as the substrate to create the microstrip antenna. The denim substrate had a thickness of 0.56 mm and a permittivity of around 1.7. Fig. 3.12 illustrates the three-layer patch antenna structure from top and side views, while table 2 outlines the optimized antenna dimensions. Both the top layer (patch) and bottom layer (ground plane) are the NC e-textile (represented in yellow), while the substrate layer (denim) is sandwiched in-between (represented in gray). To securely attach the e-textile patch to the substrate so that no air gap would be present, a very thin fusible bond material (stitch witchery) was applied between the NC fabric and the denim. Because the fusible web is very thin, its influence on antenna performance is ignored.

The antenna is designed to operate in the 2.45 GHz ISM band. The optimized antenna dimensions are given in Table 9. In order to compare the textile antenna performance with traditional antenna, we fabricated a copper antenna by using the same denim substrate and same dimension. But the conductive fabric is replaced with copper tape. Fig. 3.13 shows the fabricated prototypes of textile antenna and copper antenna. The antenna performance was tested both in free space and on human chest by a network analyzer Agilent PNL N5230C.

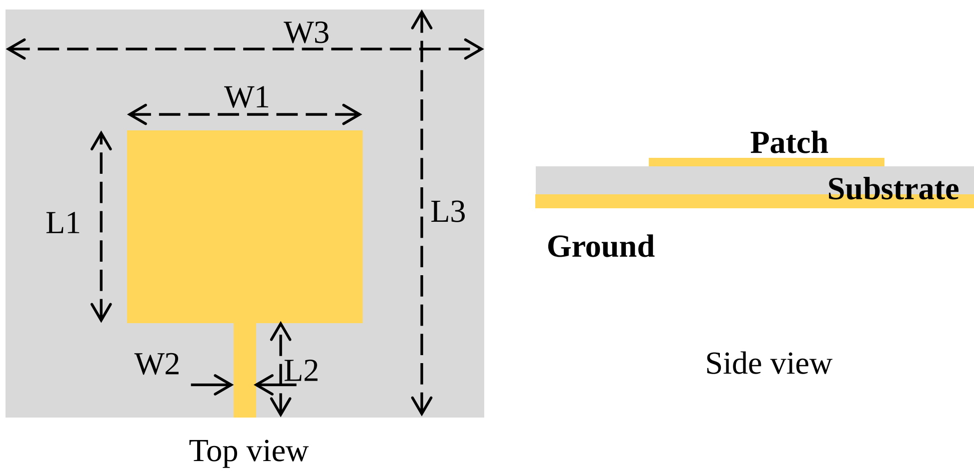

Fig. 3.12 Textile microstip antenna.

Table 9 Dimensions of the textile antenna (mm).

W1	W2	W3	L1	L2	L3
53	2	90	47	10	90

To measure antenna performance, two antenna parameters are explored for free space and human body application: reflection coefficient and realized gain. Fig. 3.14 (a) illustrate the antenna performance measurement setup in free space. The textile antenna was connected to a vector network analyzer (Agilent PNL N5230C) and acted as a transmitting antenna. A standard horn antenna acted as a receiving antenna and was placed 2 m away from the textile antenna. The vector network analyzer can measure the S_{11} and realized gain of the textile antenna. For on body test, similar setup was used except that textile antenna was mounted on the chest, as shown in Fig. 3.14 (b).

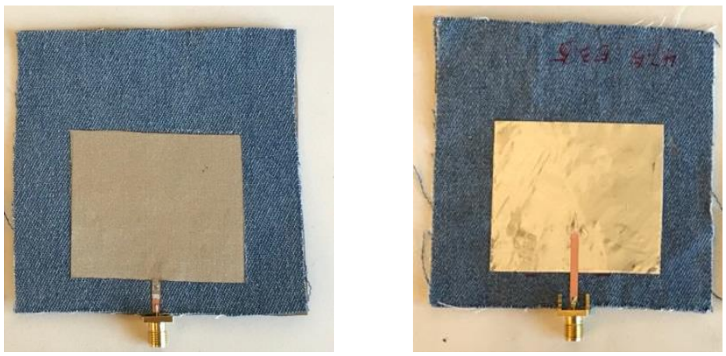

(a) (b)

Fig. 3.13 Photos of fabricated (a) textile antenna and (b) copper antenna.

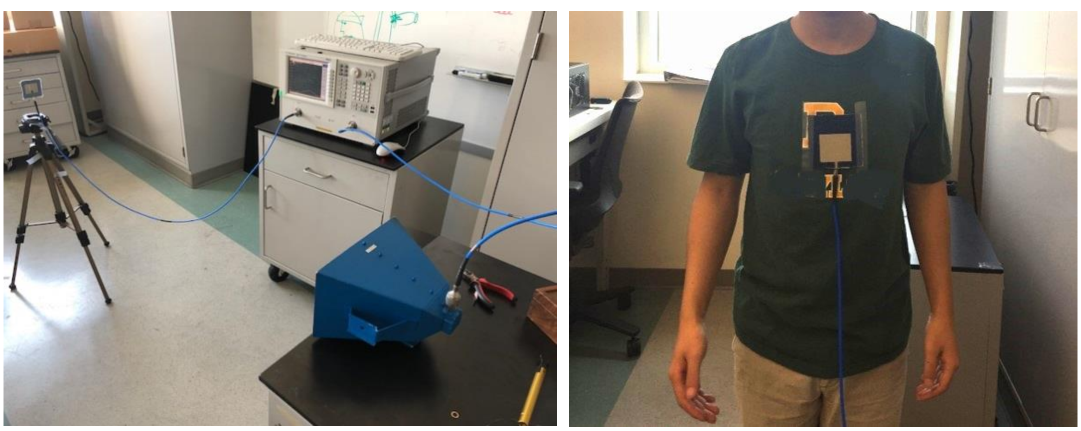

(a) (b)

Fig. 3.14 Antenna measurement setup (a) in free space and (b) on human body

Fig. 3.15 shows the measured reflection coefficients of both antennas both in free space and on human body. It can observed that both antenna resonate around 2.5 GHz. And the resonance frequency shifts when placed on human body, which is due to the high permittivity of body tissues. The textile antenna can achieve a bandwidth of 3% with S_{11} below -10 dB, which is similar with copper antenna performance.

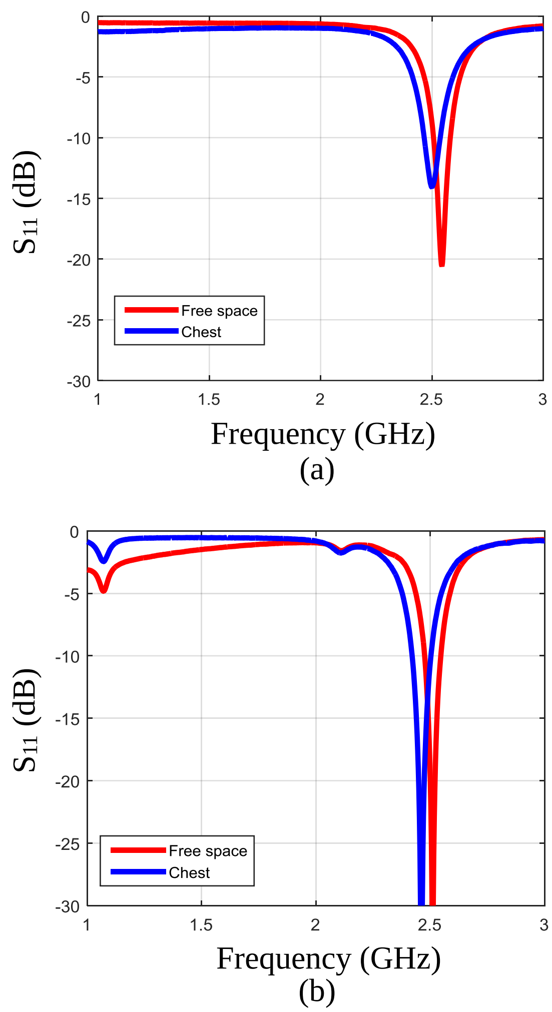

Fig. 3.15 Measured reflection coefficient of (a) textile antenna and (b) copper antenna

Fig. 3.16 plots the realized gain of both antennas. It can be observed that the textile antenna can achieve a gain of 5 dB on chest, about 2 to 3 dB lower than the antenna in free space. This is because the body tissues are lossy material. For comparison, the textile antenna can achieve comparable gain with the copper antenna.

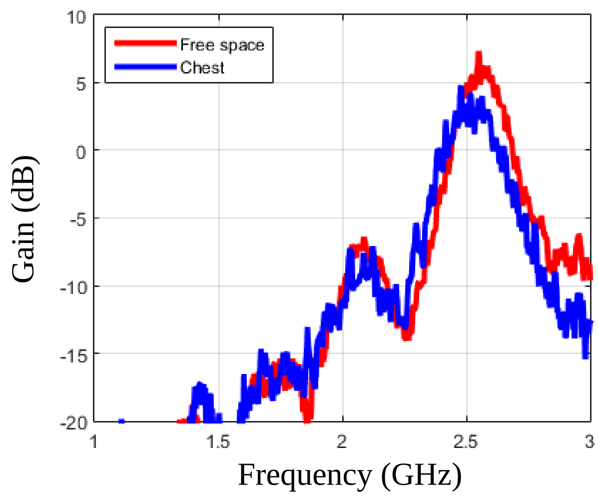

(a)

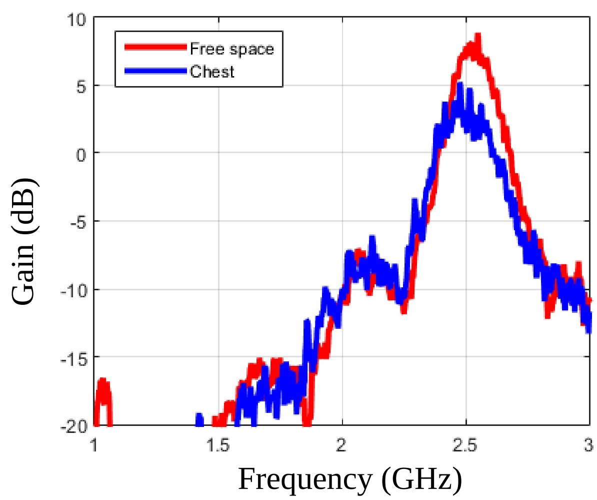

(b)

Fig. 3.16 Measured realized gain of (a) textile antenna and (b) copper antenna

3.3 Durability Test on Antenna Performance

The same durability tests were performed on textile antennas including moisture, laundry, pilling, and wrinkling test. We also performed the strain test on antenna, though we were not able to do this on the surface resistivity study, because the shape distortion caused by the strain test make it difficult to measure the surface resistivity accurately.

3.3.1 Moisture

The purpose of this test is to measure the moisture effect on antenna performance. For the moisture test, the antenna was soaked in distilled water for 10 minutes and then removed to naturally air dry under room temperature (21 ^{o}C). The antenna performance was measured twice after test. One moisture reading was taken approximately 6 hours after the initial soak, represented by the red curve in Fig. 3.17 (damp). After the antenna is completely dried a second measurement was taken (approximately 18 hours of air drying), represented by the black curve. It was found that moisture can shift the antenna resonance frequency to a lower value, due to the high permittivity of water. The presence of moisture also caused the antenna gain to drop by more than 10 dB. This is because water can absorb electromagnetic energy and cause degradation to the antenna radiation ability.

3.3.2 Laundry

This test is to measure the laundry effect on antenna performance. The AATCC method 61 was followed in this test. Although 4 different detergents were used in surface resistivity study, they didn't show significant difference. So for simplicity, only standard detergent was used in the antenna test. Similar to the moisture test, antenna performance was measured twice after the roto wash procedure. The initial measurement was taken under damp conditions (6 hours of air drying) and the second measurement was performed after the antenna was completely dry (approximately 18 hours). Fig. 3.18 shows the performance change after laundering. It was found that the antenna resonant frequency shifts from 2.5 GHz to 1.85 GHz and the gain drops by 7 dB when the antenna is damp. This is because water increases the permittivity and loss tangent of the denim substrate. After completely dried, the antenna shows a similar performance as before conducting the roto wash procedure.

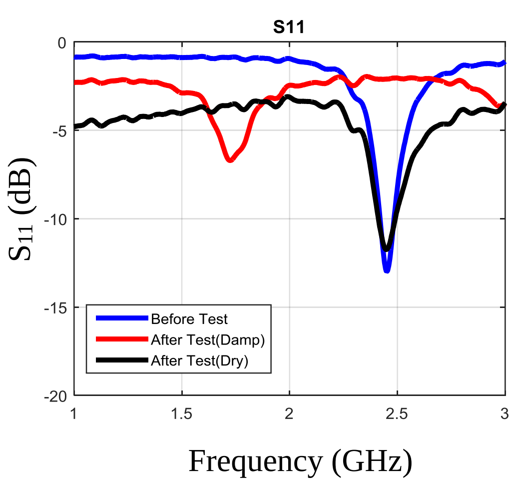

(a)

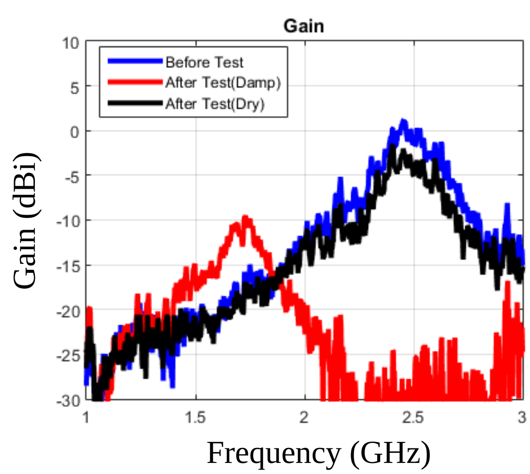

(b)

Fig. 3.17 Moisture effect on antenna performance: (a) S_{11} and (b) realized gain

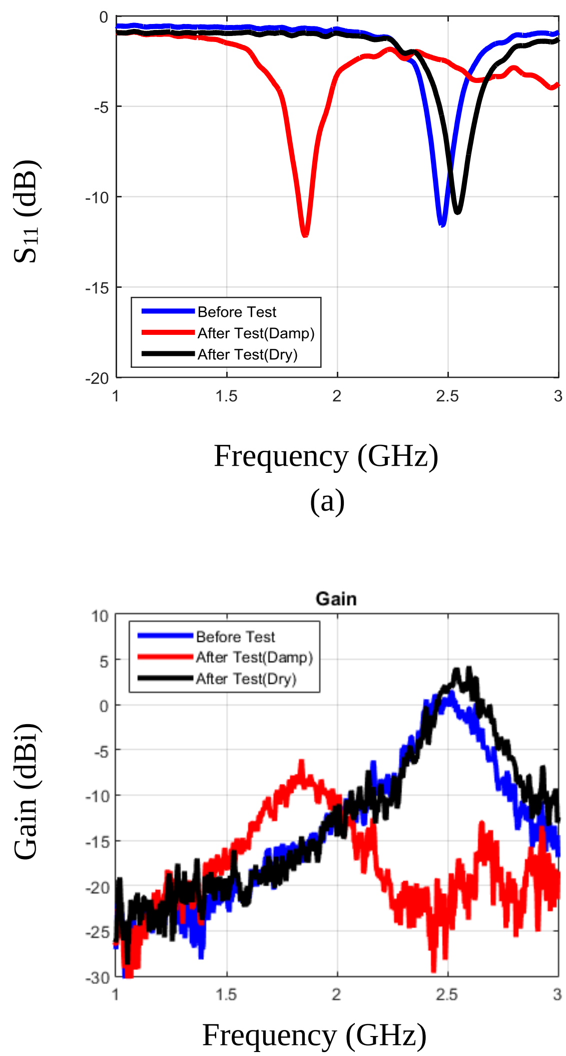

(a)

(b)

Fig. 3.18 Laundry effect on antenna performance: (a) S_{11} and (b) realized gain

3.3.3 Pilling

The purpose of this test is to measure the pilling effect on antenna performance. The ASTM D3512 was followed for this test. Fig. 3.19 (a) and (b) illustrate the antenna appearance change before and after the pilling test. Fig. 3.20 (a) shows the antenna reflection coefficient (or S_{11}), where blue and red curves represent antenna performance pre- and post-pilling test. The blue curve has a dip around 2.5 GHz, indicating that the antenna resonates at around 2.5 GHz. The resonance disappears after the pilling test. Fig. 3.20 (b) shows the measured antenna gain. It was found that the gain drops almost by 20 dB. Thus, it is be suggested that pilling due to normal wear may cause severe damage to antenna performance. Findings agree with the DC resistivity study that NC fabric becomes non-conductive after pilling test.

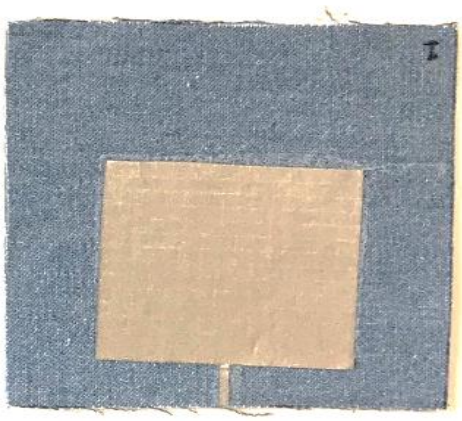

(a)

(b)

Fig. 3.19 Photos of textile antenna (a) pre- and (b) post-pilling test.

3.3.4 Wrinkle

This test is to measure the wrinkle effect on antenna performance. The AATCC 128 was followed for this test. Fig. 3.21 shows the antenna appearance before and after the wrinkling test, indicating harsh wrinkle lines (particularly on the patch). Some wrinkles can be clearly seen on Fig. 3.21 (b). Fig. 3.22 shows the antenna performance change pre-and post-wrinkling test. It is found that the resonant frequency doesn't change and the antenna gain only drops by 2 dB.

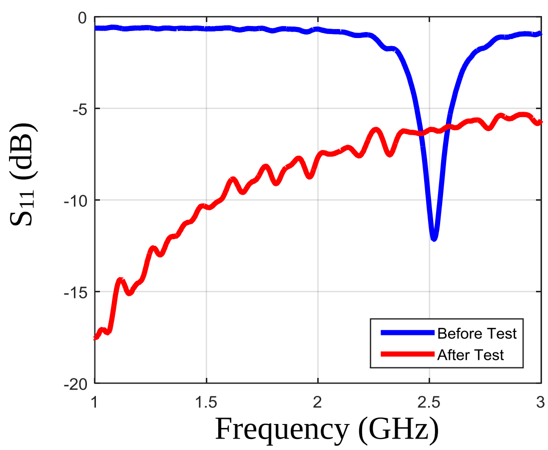

(a)

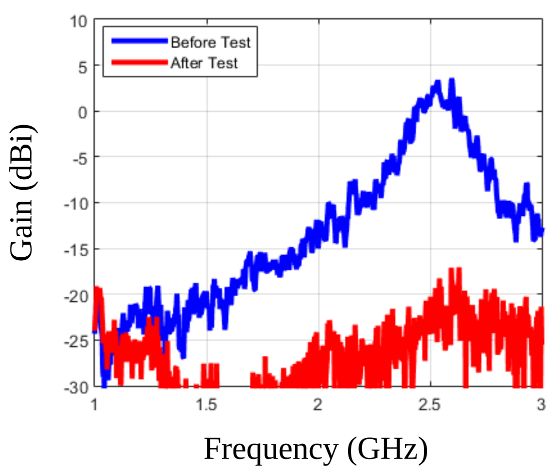

(b)

Fig. 3.20 Pilling effect on antenna performance: (a) S_{11} and (b) realized gain.

(a)

(b)

Fig. 3.21 Photos of textile antenna (a) pre- and (b) post-wrinkle test.

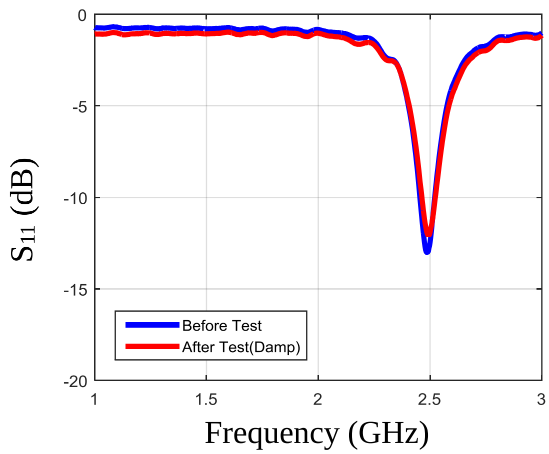

(a)

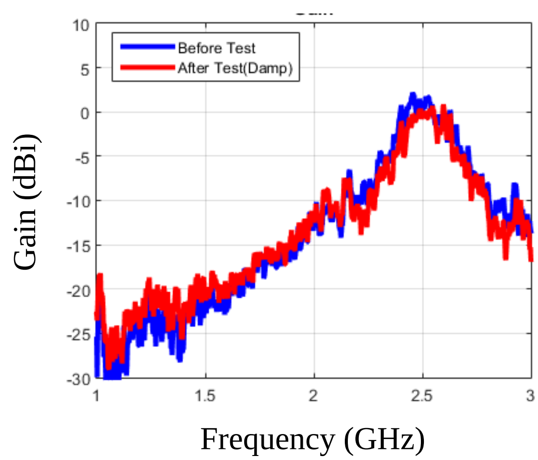

(b)

Fig. 3.22 Wrinkle effect on antenna performance: (a) S_{11} and (b) realized gain.

3.3.5 Strain

The purpose of this test is to measure the strain effect on antenna performance. The ASTM D5034 was followed in this test. In this test, the antennas were pulled in vertical and horizontal directions respectively. Fig. 3.23 shows the antenna photos after test. It can be observed that the patch size in the pulling direction clearly increased (by approximately 1-3 mm). Fig. 3.24 and 3.25 illustrate the antenna performance change after it was pulled vertically and horizontally in separate tests. It is found that pulling the patch antenna vertically decreased the resonance frequency (as shown in Fig. 3.24 (a)), as the side length L increased, which directly determined the resonance frequency. The gain dropped about 5 dB (as shown in Figure 3.24 (b)), because the e-textile tear near the antenna input port blocked the electrical current. On the other hand, when antenna was pulled horizontally, its resonance frequency shifted higher (as shown in Fig. 3.25 (a)). This is because the side length L shrunk after being pulled horizontally. The gain did not show substantial change.

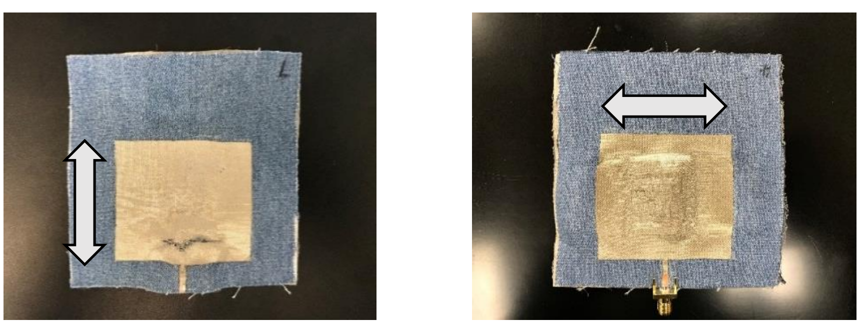

(a) (b)

Fig. 3.23 Photos of textile antennas after being pulled (a) vertically and (b) horizontally.

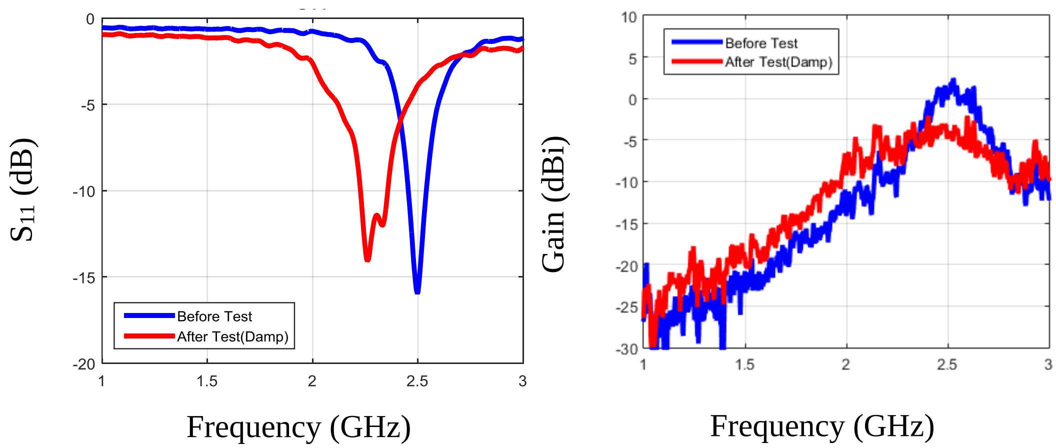

(a) (b)

Fig. 3.24 Textile antenna (a) S_{11} and (b) realized gain before and after being pulled vertically

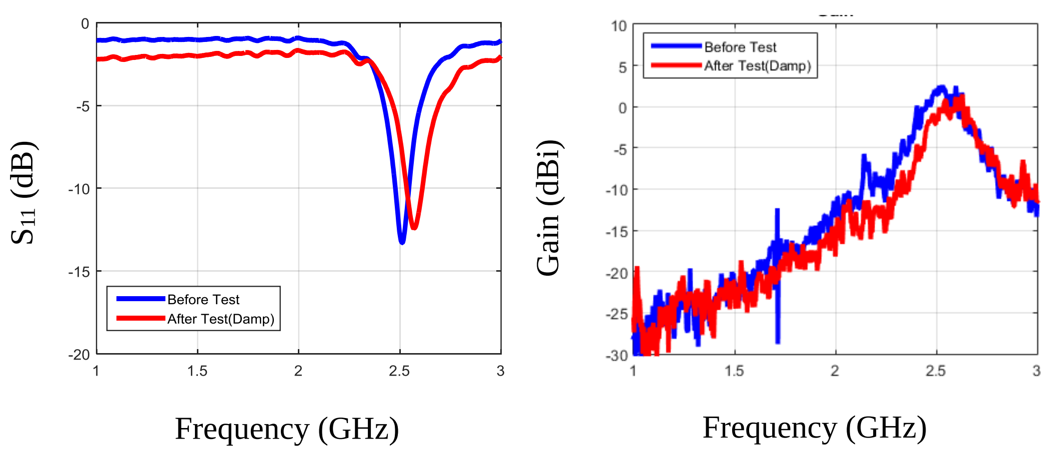

(a) (b)

Fig. 3.25 Textile antenna (a) S_{11} and (b) realized gain before and after being pulled horizontally

3.4 Summary

In this chapter, e-textile performance under different harsh wear conditions was investigated from both DC and RF perspectives. It was found that pilling and abrasion caused a substantial change to the e-textile conductivity and antenna (both NC e-textile and copper tape) performance, which may cause wearable devices that utilize these materials to lose communication. Wrinkling can slightly increase its surface resistivity and cause the antenna gain to drop only by 2 dB. Laundering and moisture can temporarily cause the antenna resonant frequency to shift lower and the gain to drop before antenna is dried, but its performance will return to normal after dry. Pulling the antenna can change its resonance frequency and slightly affect its gain.

Findings of this study provide insight for the integration of e-textile antennas into WBAN and wearables. Harsh wear conditions tested in this study provide important information on the performance capabilities and limitations for potential applications in military, sports and/or wellness industries. While complete e-textile challenges still exist for integration in the market of wearables, results of this study provide understanding and optimism for designing and implementing wearable antennas that are low profile, lightweight, and flexible.

CHAPTER FOUR

Human Body Dynamic Motion Measurement and Classification Results

Portion of this chapter was published as a article that I jointly authored:[86]

In this chapter, we will discuss several human body dynamic motion experiments that we conducted by using the three wearable antennas that we designed in previous chapters. The dynamic motion measurements include finger motions, head movements, mouth activities, and arm motions. Dynamic time warping (DTW) algorithm was applied to classify finger motions.

4.1 Finger Dynamic Experiment and Results

In this section, we conducted the finger motion experiments using the 2 above designed wrist-worn FCH antennas. Antenna A works at 890 MHz and Antenna B works at 2.45 GHz. In our experiment setup, the FCH antennas were mounted on the left wrist of a participant and connected to a vector network analyzer (Agilent PNL N5230C) using a coaxial cable. The antenna reflection coefficients at its resonance frequency were recorded as the subject performs different finger motions using either the left hand or the right hand, as described below.

4.1.1 Finger Motion of the Right Hand

Fig. 4.1 illustrates the 4 finger gestures that were performed in the test: click, swipe, zoom, and circle of the left hand index finger. The antenna is attached on the left wrist. These finger activities are commonly used for wireless controls and human-computer interactions. Each motion is repeated once per second and iterated for 20 seconds. Four volunteers, including two males and two females, are included in the experiment. As an example, Fig. 4.2 and Fig. 4.3 illustrate the magnitude and phase of the measured reflection coefficients of Antenna A, while Fig. 4.4 and Fig. 4.5 show the reflection coefficients of Antenna B. It can be observed that the magnitude variation for Antenna A is around 0.5 to 1 dB greater and the phase variation is about 4 to 10 degree greater than that of Antenna B as a person performs the left index finger motions.

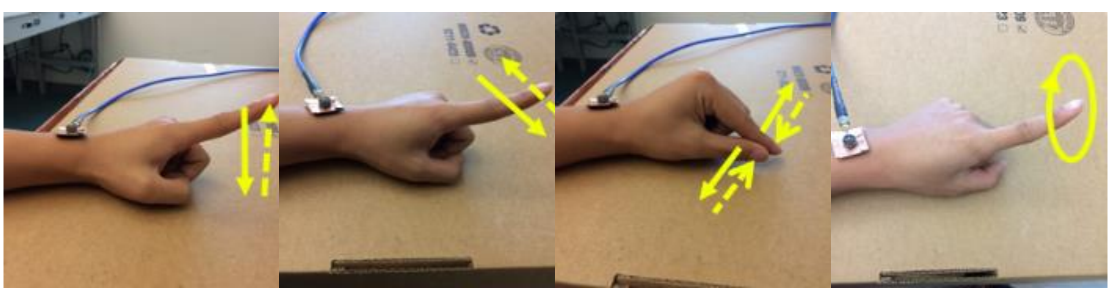

(a) (b) (c) (d)

Fig. 4.1 (a) Click, (b) swipe, (c) zoom, and (d) circle of the left index finger

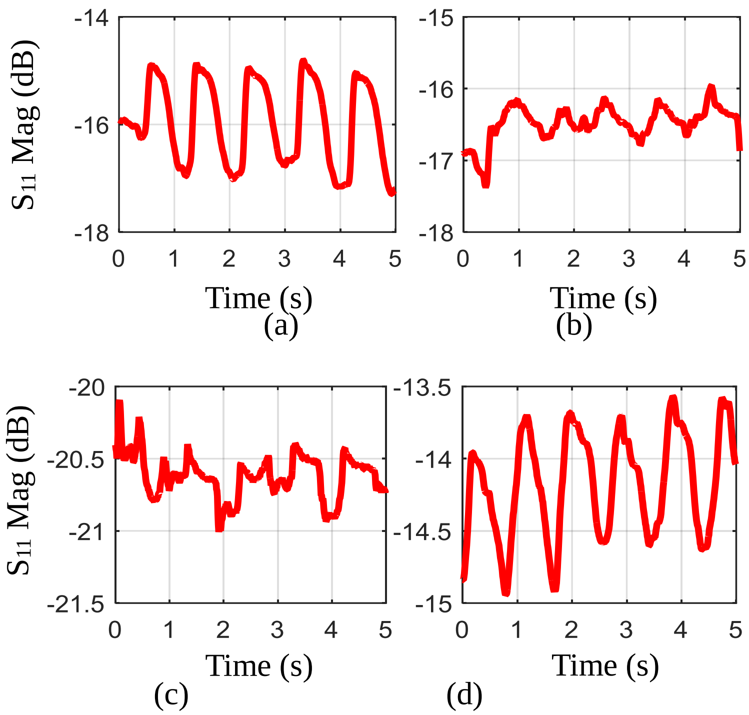

Fig. 4.2 S_{11} magnitude of the Antenna A for (a) click, (b) swipe, (c) zoom, (d) circle.

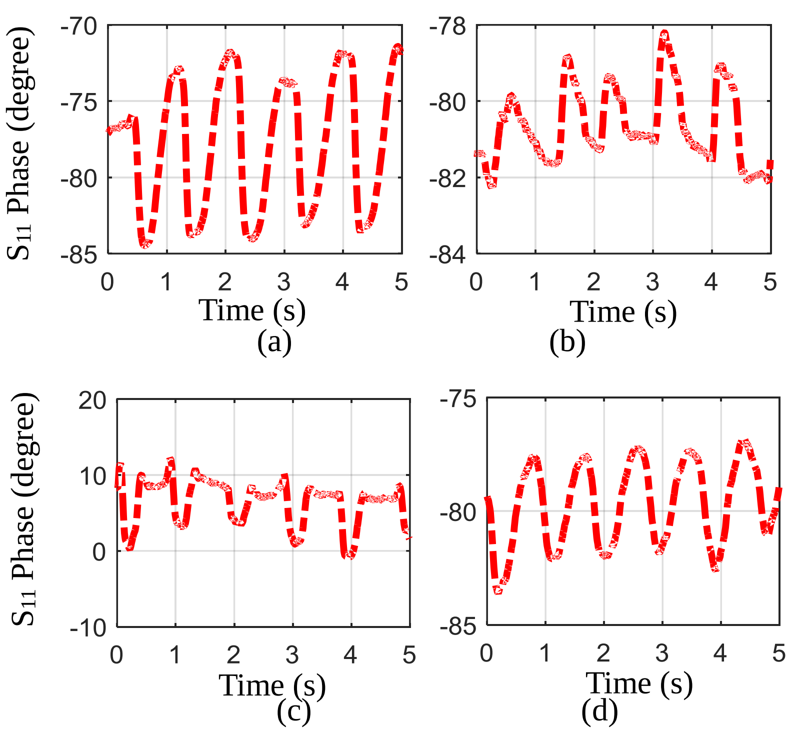

Fig. 4.3 S_{11} phase of the Antenna A for (a) click, (b) swipe, (c) zoom, (d) circle.

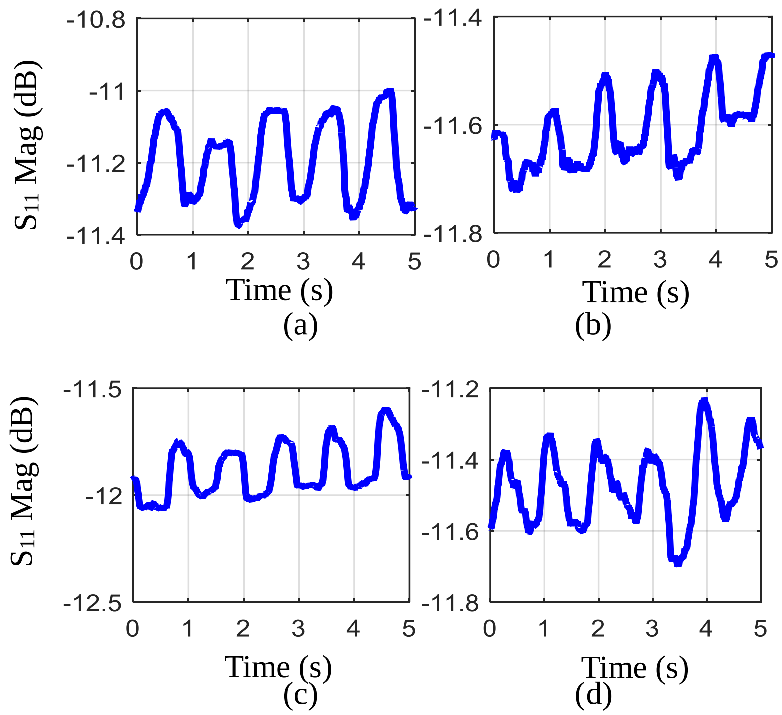

Fig. 4.4 S_{11} magnitude of the Antenna B for (a) Click, (b) swipe, (c) zoom, (d) circle.

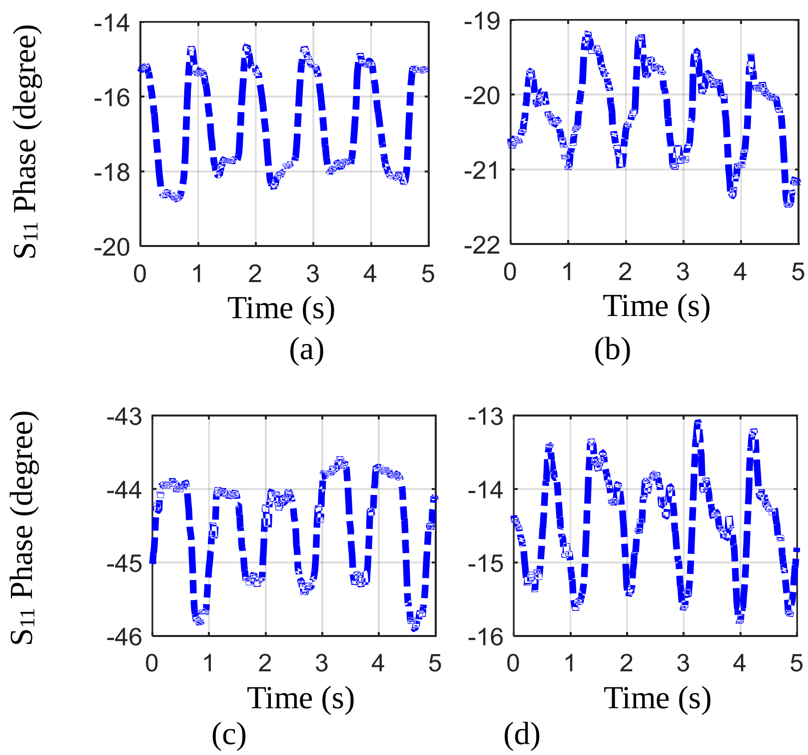

Fig. 4.5 S_{11} phase of the Antenna B for (a) click, (b) swipe, (c) zoom, (d) circle.

4.1.2 Finger Motion of the Right Hand

In the second setup, we measure click, double click, zoom and circle motions of the right hand index finger of which movement is carried out near the antenna attached to the left wrist, as shown in Fig. 4.6. Similarly, each motion is repeated once per second and iterated for 20 seconds. Two volunteers, including one male and one females, are included in the experiment.

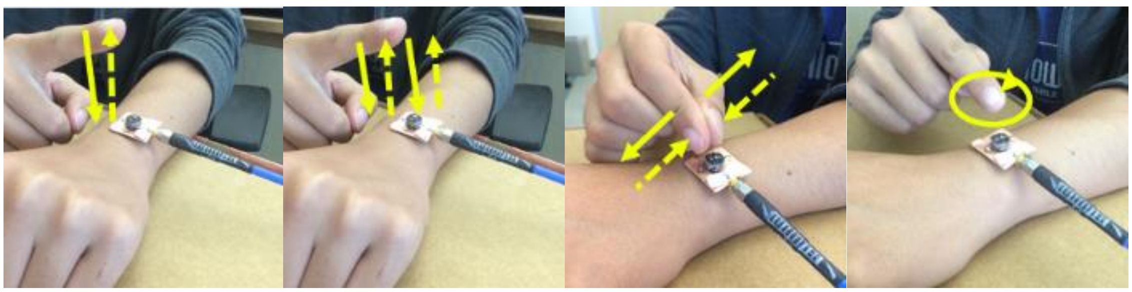

(a) (b) (c) (d)

Fig. 4.6 (a) Click, (b) double click, (c) zoom, and (d) circle of the right index finger.

Compared to the left hand finger movements, the right index finger motions cause a much larger variation on both magnitude (up to 20 dB) and phase (up to 150 degrees) for both Antenna A and Antenna B, as can be seen from Fig. 4.7 to Fig. 4.10. This is because the right index finger motion is much closer to the antenna, causing larger perturbation of the near fields. Overall, both the magnitude and phase show unique patterns for different finger activities, which can be utilized for recognition purposes.

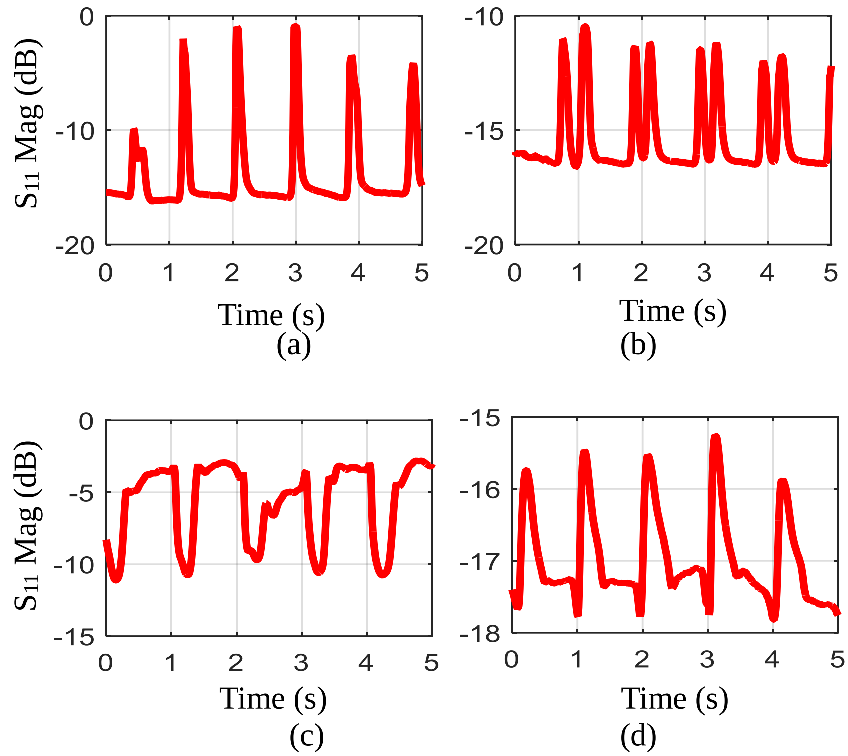

Fig. 4.7 S_{11} magnitude of the Antenna A for (a) click, (b) double click, (c) zoom, (d) circle.

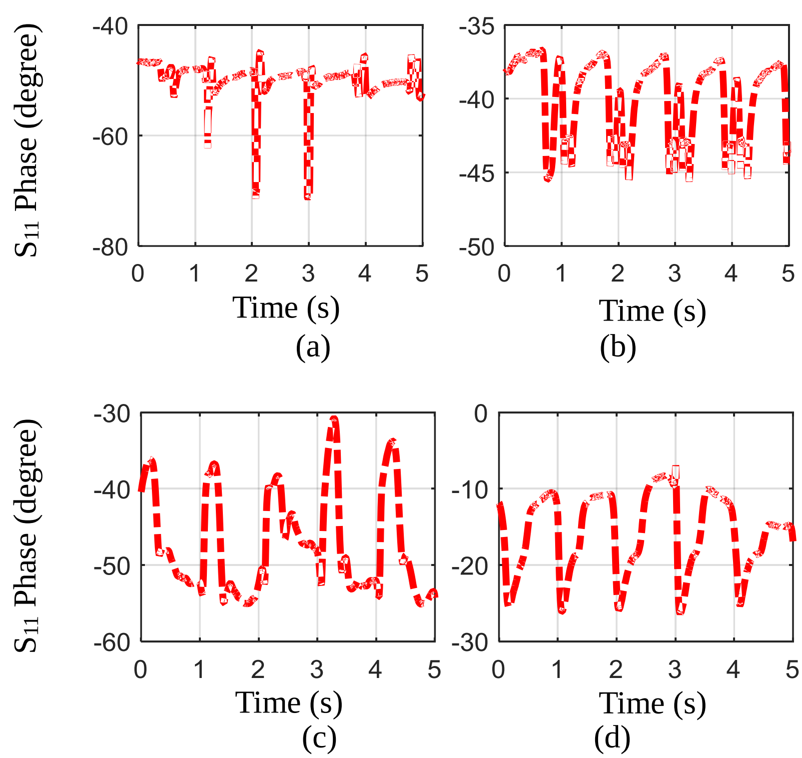

Fig. 4.8 S_{11} Phase of the Antenna A for (a) click, (b) double click, (c) zoom, (d) circle.

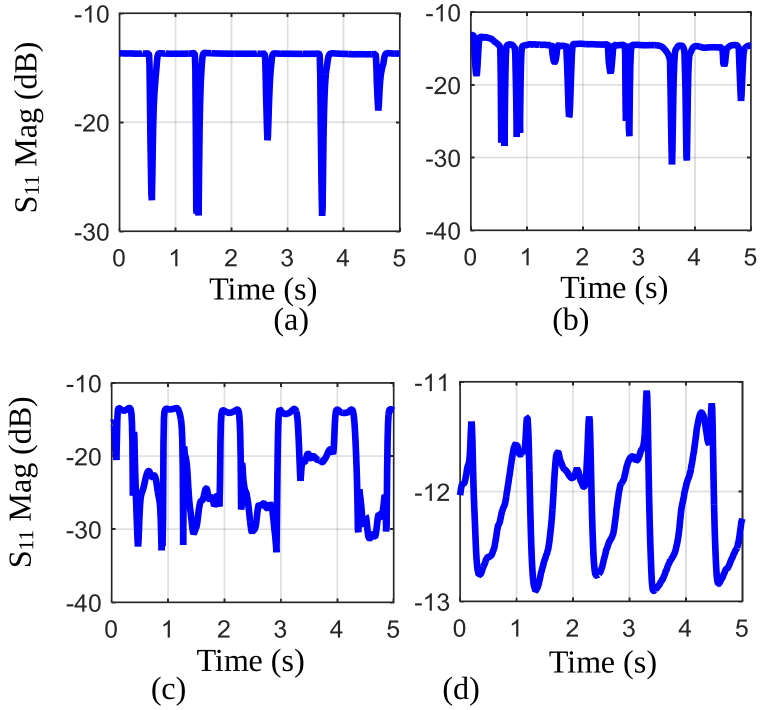

Fig. 4.9 S_{11} magnitude of the Antenna B for (a) click, (b) double click, (c) zoom, (d) circle.

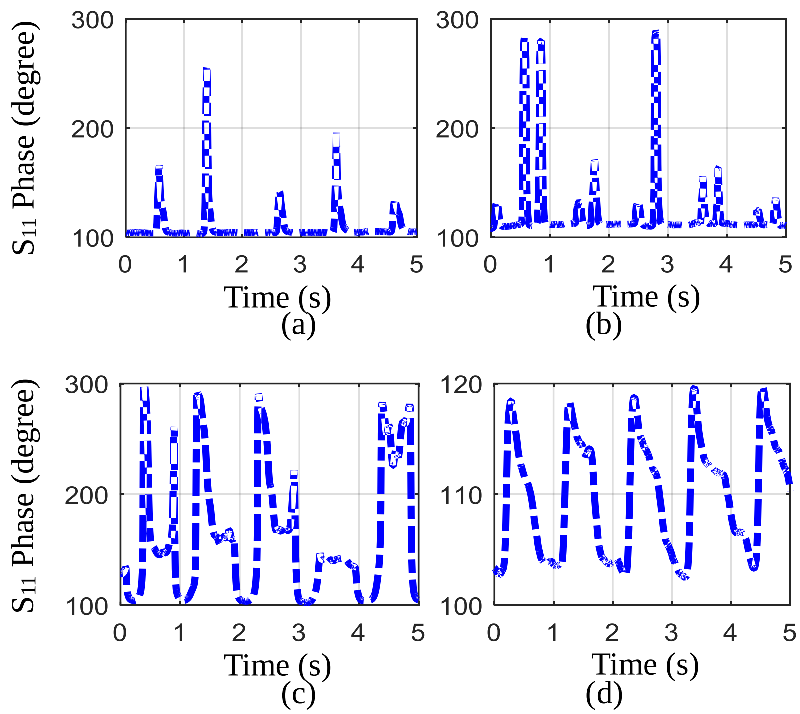

Fig. 4.10 S_{11} phase of the Antenna B for (a) click, (b) double click, (c) zoom, (d) circle.

4.2 Head and Mouth Dynamic Experiment and Results

In this section, we conducted the finger motion experiments using a button-shape end-fire FCH antenna array, as shown in Fig. 2.18. The antenna design was introduced in Chapter 2.2. In the experiment setup, the FCH antenna array was mounted on the chest of a participant and connected to a vector network analyzer (Agilent PNL N5230C) using a coaxial cable, as shown in Fig. 2.20. The antenna reflection coefficients at its resonance frequency were recorded as the subject performs different head and mouth movements.

4.2.1 Mouth Movements

Four mouth activities were performed in the test: eating, drinking, coughing, and speaking. These are most common happened mouth activities in everyday life. Each motion is iterated for 120 seconds. Four volunteers, including two males and two females, are included in the experiment. As an example, Fig. 4.11 and Fig. 4.12 illustrate the magnitude and phase of the measured reflection coefficients of the antenna. For clarity, only 10 s of recorded data is presented. It can be observed that the magnitude variation is around 1 to 4 dB. Among the 4 activities, speaking shows the least magnitude variation, because the movement magnitude for speaking is the smallest. The phase variation for eating and drinking is about 5 degree greater than that of speaking, which is only around 2 degree. Cough exhibits the biggest magnitude and phase variation, because cough is the biggest movement.

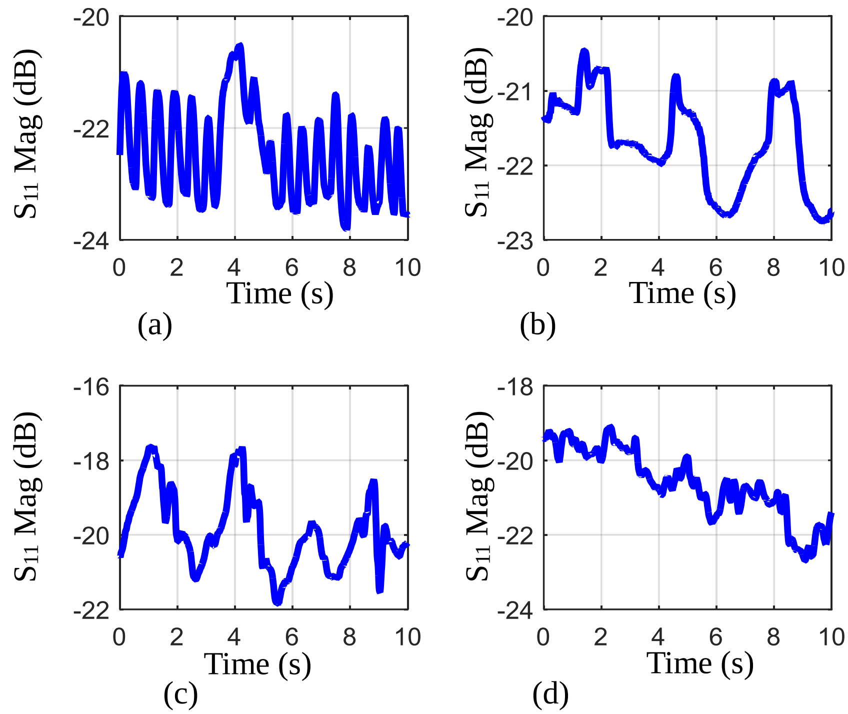

Fig. 4.11 S_{11} magnitude of the antenna when the subject performed (a) eating, (b) drinking, (c) cough, (d) speaking.

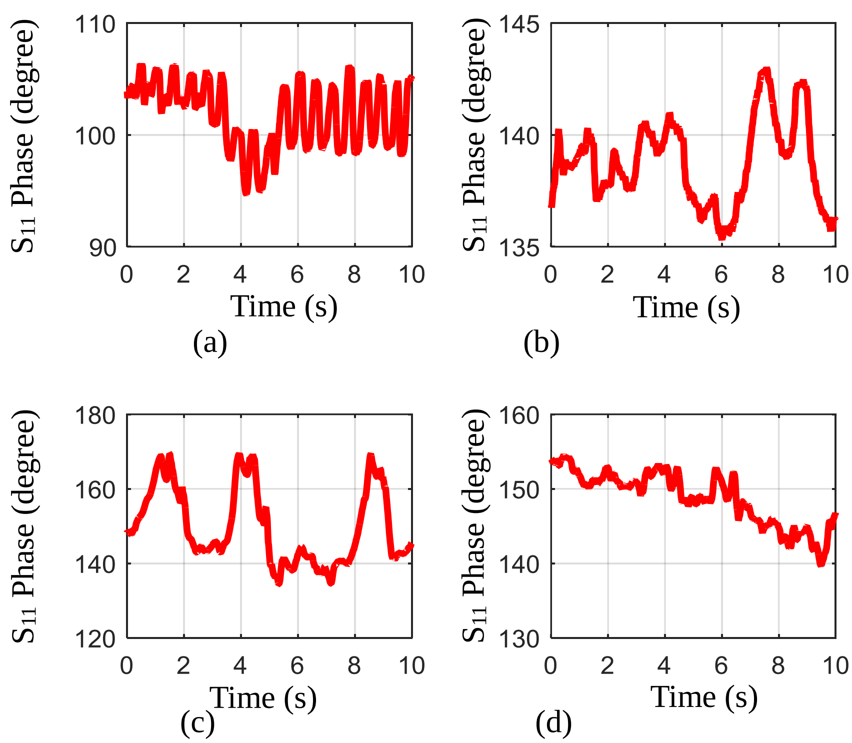

Fig. 4.12 S_{11} phase of the antenna when the subject performed (a) eating, (b) drinking, (c) cough, (d) speaking.

4.2.2 Head Movements

Fig. 4.13 illustrates the 3 head activities that we performed in the test: side-to-side, left-and-right, back-and-forth. Each motion is iterated for 120 seconds. Four volunteers, including two males and two females, are included in the experiment. As an example, Fig. 4.14 and Fig. 4.15 illustrate the magnitude and phase of the measured reflection coefficients of the antenna. For clarity, only 10 s of recorded data is presented. It can be observed that the magnitude variation is around 2 dB. It can be observed that different activities show different patterns. The phase variation is about 10 to 15 degree.

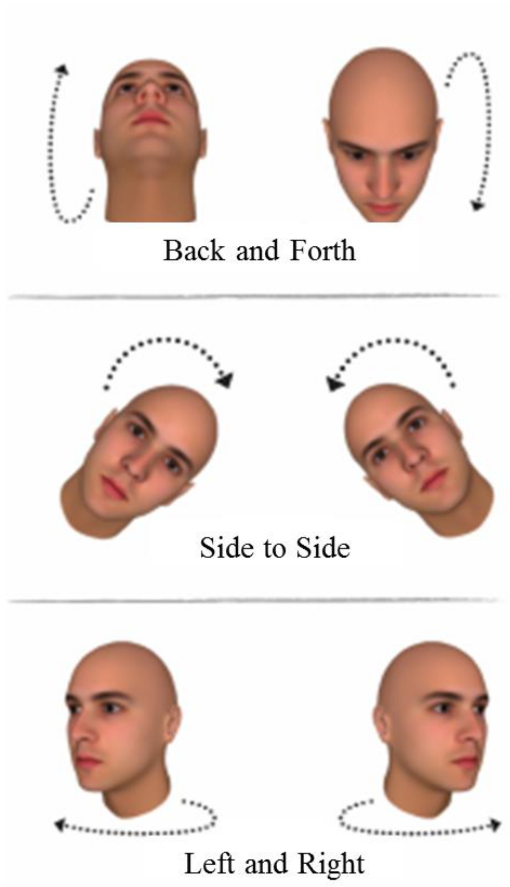

Fig. 4.13 Head movement dynamic experiments

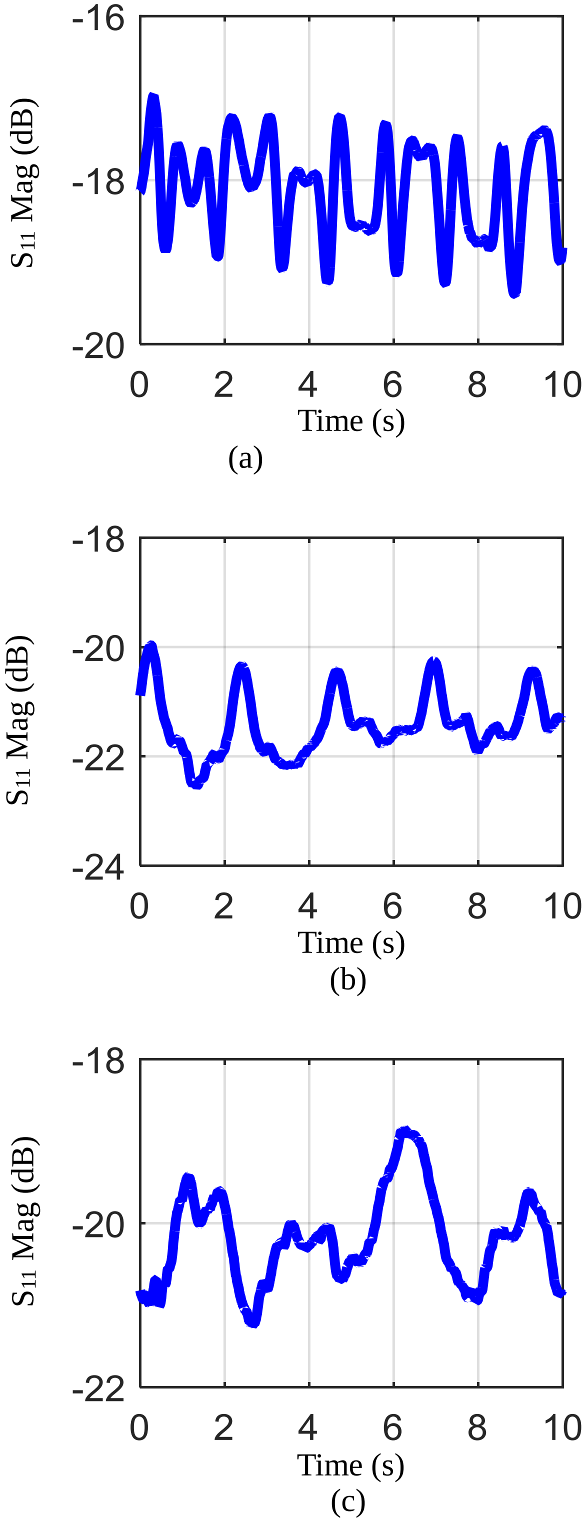

Fig. 4.14 S_{11} magnitude of the antenna when the subject performed (a) back-and-forth, (b) side-to-side, (c) left-and-right movements.

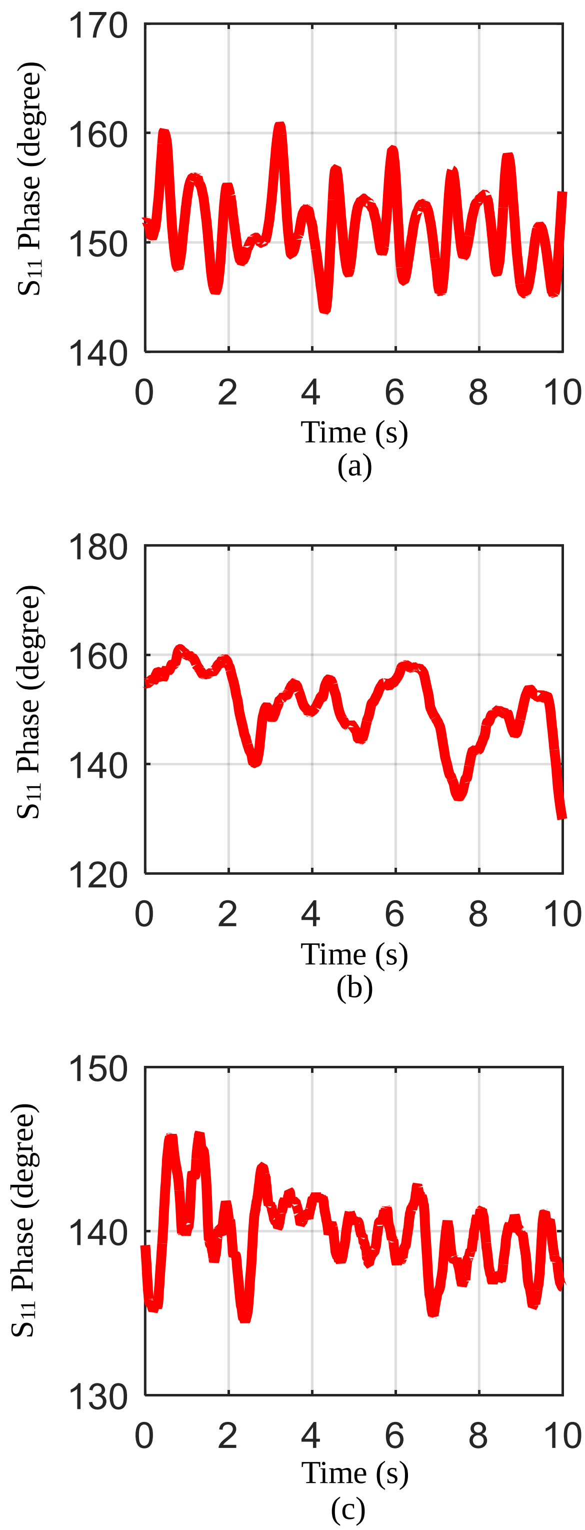

Fig. 4.15 S_{11} phase of the antenna when the subject performed (a) back-and-forth, (b) side-to-side, (c) left-and-right movements.

4.3 Arm Dynamic Experiment and Results

In this section, we conducted the arm dynamic experiments using the wearable e-textile antenna which is introduced in Chapter 3.2, as shown in Fig. 3.13 (a). In the experiment, the textile antenna was mounted on the right side of a participant's upper body and connected to a vector network analyzer (Agilent PNL N5230C) using a coaxial cable, as shown in Fig. 4.16.

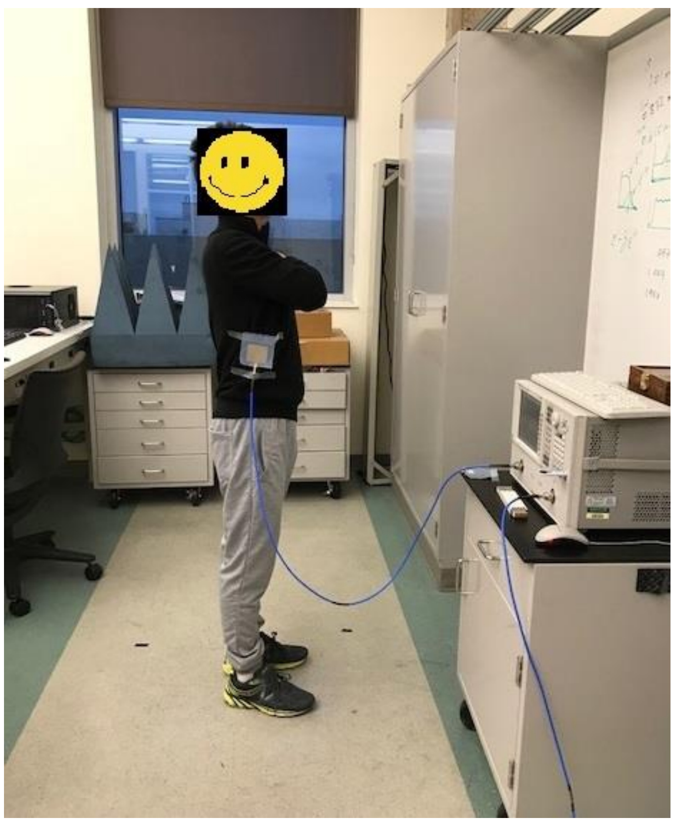

Fig. 4.16 Arm dynamic experiment.

Before conducting the arm dynamic experiment, the reflection coefficient of the textile antenna was measured, as illustrated in Fig. 4.17. It can be seen that the antenna resonates around 2.52 GHz and it can achieve a bandwidth of 6.4% with S_{11} below -10 dB. To do the arm dynamic experiment, the VNA was changed to continuous wave mode. Under this mode, the VNA continuously transmits a continuous wave at a fix frequency for a pre-set period. The wave frequency was set at 2.52 GHz, the resonance frequency. The sweep time was 60 second and a total of 14400 points was recorded for a single sweep.

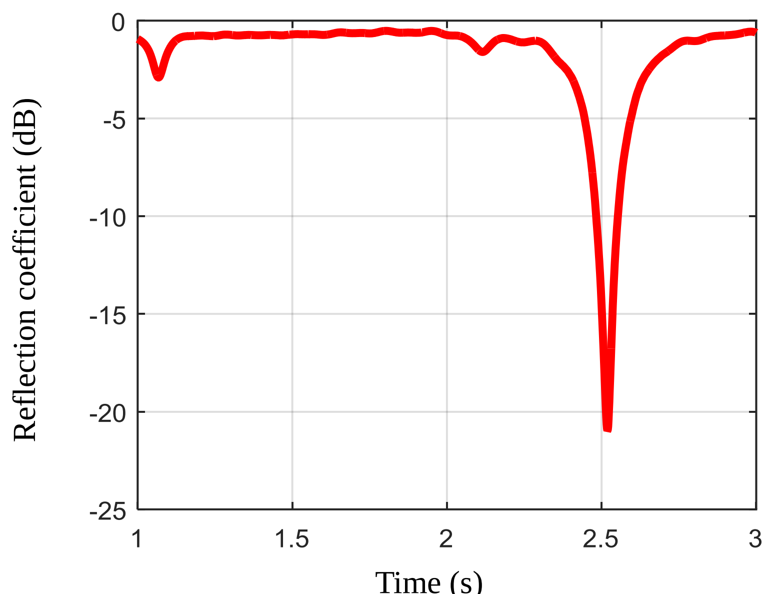

Fig. 4.17 Measured S_{11} of textile antenna worn on upper body

Fig. 4.18 illustrates the 4 different arm activities that we performed in the experiment: arm swing, arm lifting, boxing, and picking-up. Four volunteers, including two males and two females, are included in the experiment. As an example, Fig. 4.19 and Fig. 4.20 illustrate the magnitude and unwrapped phase of the measured reflection coefficients of the textile antenna when one subject perform those four arm motions. It is found that arm swing and picking-up can result in the antenna S_{11} a magnitude variation of around 10 dB, while arm lifting and boxing caused a variation of around 5 dB. This is because arm-swing and picking-up caused a bigger perturbation on the antenna near field distribution. Similarly, the biggest phase variation is also caused by the picking-up action, up to 100 degree variation.

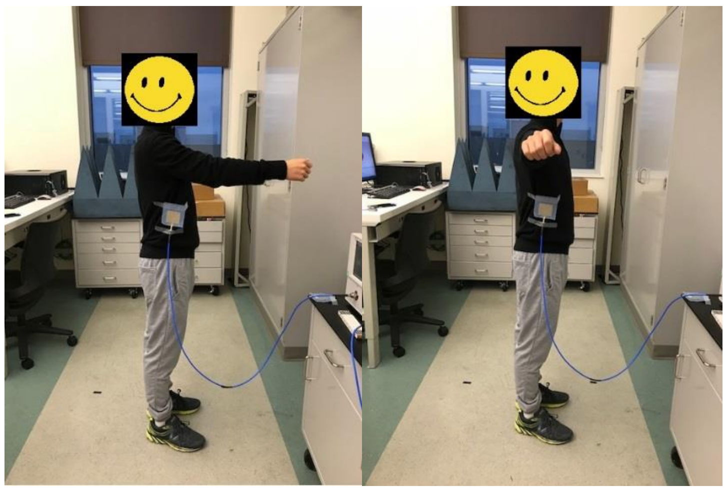

(a) (b)

(c) (d)

Fig. 4.18 Arm activities: (a) arm swing, (b) arm lifting, (c) boxing, (d) picking-up

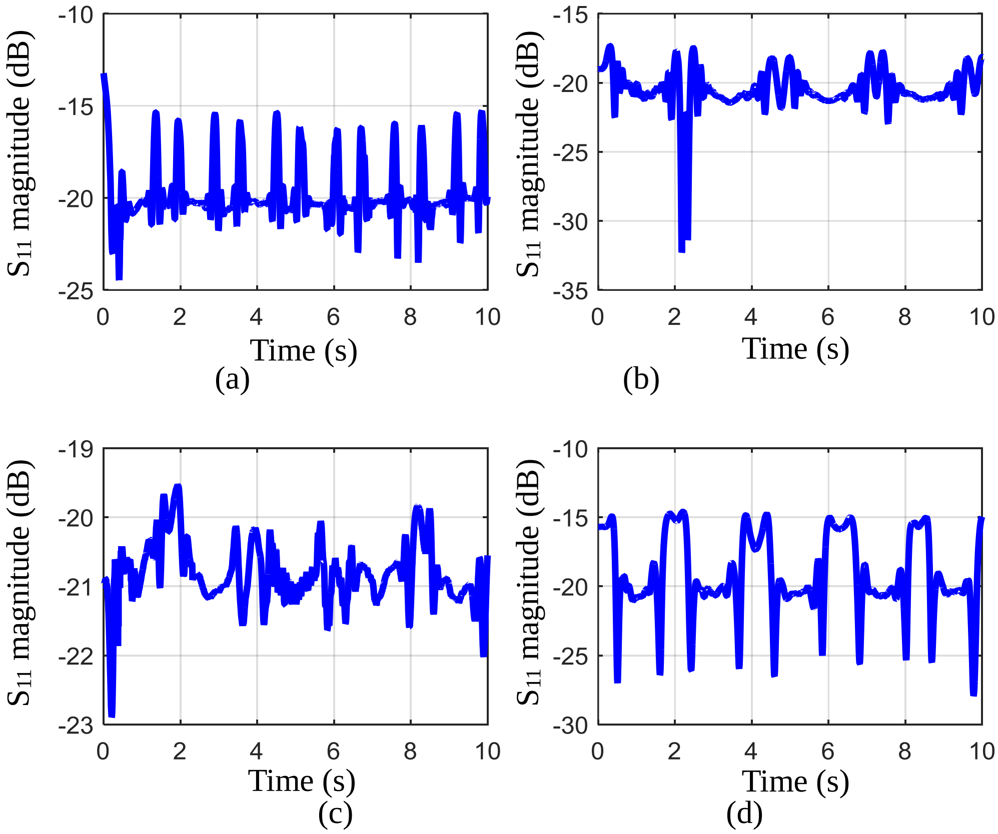

Fig. 4.19 S_{11} magnitude of the antenna when the subject performed (a) arm swing, (b) arm lifting, (c) boxing, (d) picking-up.

4.4 Classification Results of Finger Motions Using DTW Algorithm

In this section, we present the dynamic time warping (DTW) technique, which has previously been applied for body posture classification study [18], to classify different finger motions. DTW calculates the similarity of two temporal signals. The signals may have linear or nonlinear variations in time, such as time delay or advance. However, DTW can compensate the time variation by aligning the two signals optimally in time. So this algorithm is very suitable to classify different body motions, considering the body motions may be performed at different rates. Fig. 4.21 illustrates how the DTW algorithm calculates the similarity of two signals. X and Y represent two signal sequences. The DTW creates a local cost matrix. It searches the optimum path from the first sample to the last in order to achieve the minimum cost. The cost function is defined by a sum of the local distance values of all cells over the path. In this way, it can compensate the non-linear variation of the two signals in time domain.

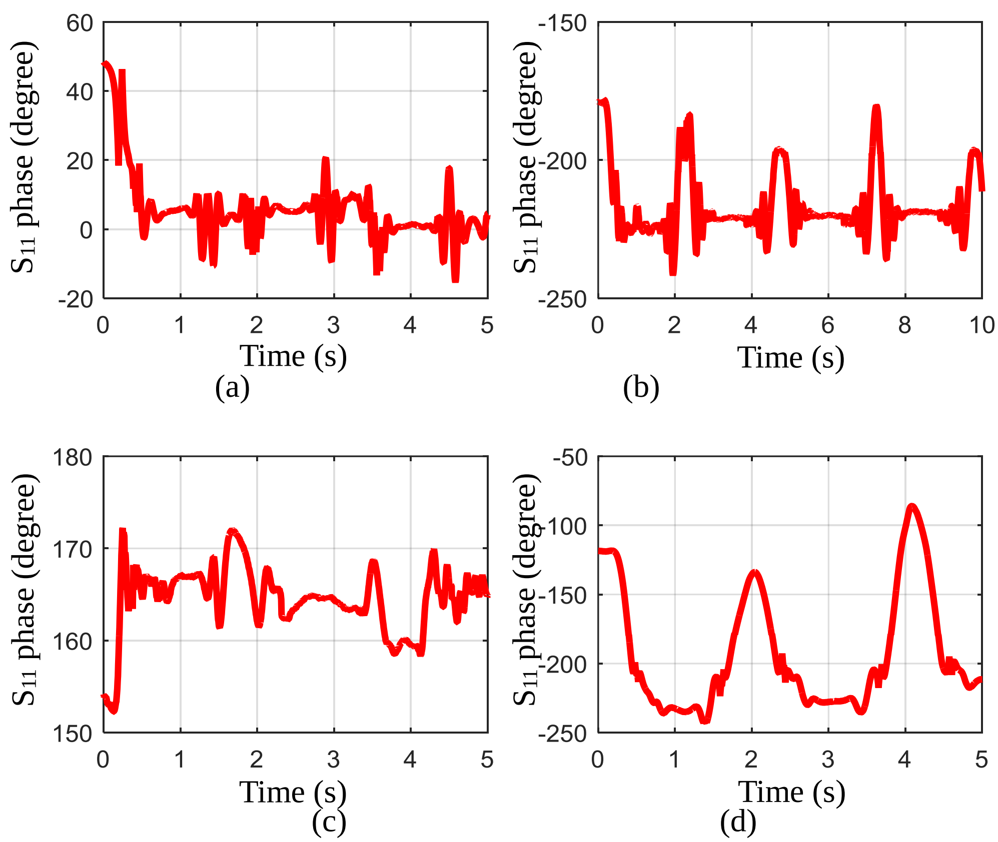

Fig. 4.20 S_{11} phase of the antenna when the subject performed (a) arm swing, (b) arm lifting, (c) boxing, (d) picking-up.

In particular, the DTW can process multi-dimensional data, which enables us to use both the magnitude and phase of S_{11} for the DTW inputs. To implement the DTW algorithm, the measured S_{11} signal should be compared with the reference signals that represent generalized signatures. Three randomly selected reference signals are used that should not be biased by a certain reference signal. Because the DTW provides the Euclidean distance between two signals, we can determine the class by identifying the reference signal that has the minimum distance to the measured signal.

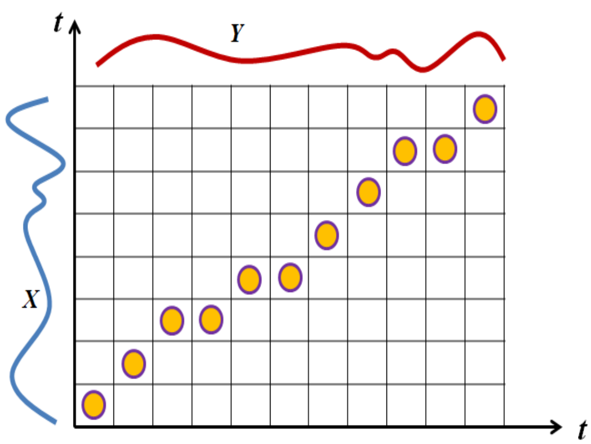

Fig. 4.21 Local cost matrix and a warping path between two signals

Because we have four participants performing four finger gestures for the first scenario, a total of 320 s (4 × 4 × 20) data are available for testing, whereas for the second scenario, a total of 160 s data are available from two participants performing four finger gestures. From each measured 20 s data, we randomly crop 20 samples using a time window. Because each finger motion has a 1 s period, we need to classify the motion using a 1 s time window.

Using the DTW as a classifier, the results are shown in Fig. 4.22 for both scenarios. In all cases, both types A and B FCH antennas can provide classification accuracies above

80%. For comparison, the type A antenna shows a higher classification accuracy for both scenarios, indicating a higher accuracy using the lower frequency FCH antenna. In addition, the second scenario shows better result than the first scenario, especially using the type A antenna.

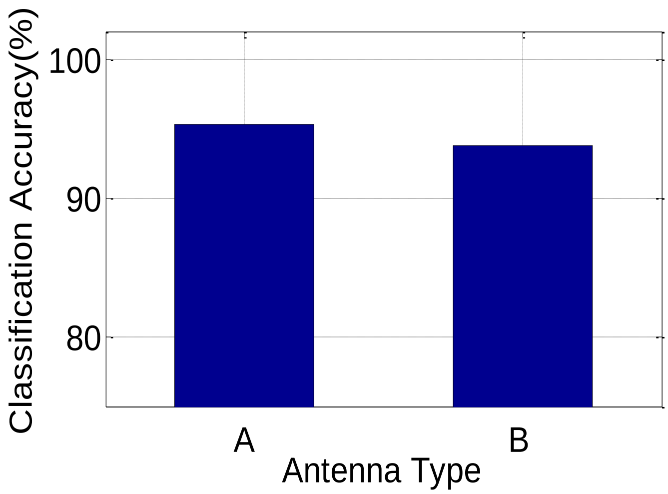

(a)

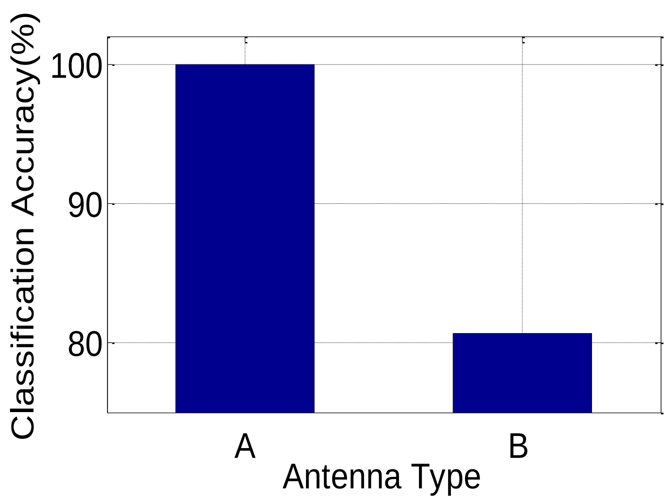

(b)

Fig. 4.22 Classification accuracy of the different antenna types. (a) First scenario. (b) Second scenario.

To investigate the necessary time-window size to obtain acceptable classification accuracy, we varied the window from 0.1 to 3 s. In general, a larger time window increases the classification accuracy because the signatures would be repeatedly included, whereas longer time is needed to acquire the data. The classification accuracies with the time window for the types *A* and *B* antennas are shown in Fig. 3.12 (a). The blue solid line denotes the result of the type *A* antenna, and the red dashed line denotes the result of the type *B* antenna. We can observe that the overall classification accuracy of the type *A* antenna is higher than that of the type *B* antenna. This result is expected because the near-field intensity of the type *A* antenna is larger, as shown in Fig. 2.4. The accuracy saturates to approximately 97% and 95%, respectively, when the window size is more than 1.5 s. For the second scenario, the classification accuracy with the time window is shown in Fig. 4.23 (b). We observe that the type *A* antenna shows the best performance with approximately 100% accuracy.

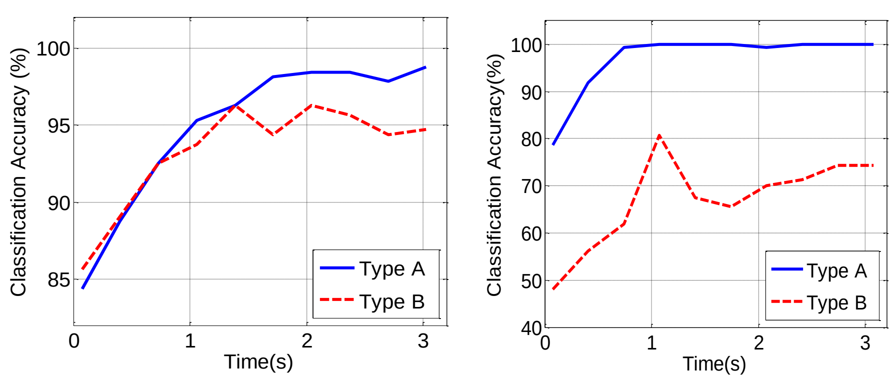

(a) (b)

Fig. 4.23 Classification accuracy with the time-window size (a) first scenario and (b) second scenario

4.5 Summary

In this chapter, we conducted 4 different body dynamic experiments, including finger, mouth, head and arm motions and finger motions. It is found that different body activities will cause different S_{11} variation patterns, because of the perturbation effect of antenna near field distribution. The DTW algorithm were applied to classify different finger motions. The classification results indicate that classification accuracy can reach up to 97% for the left index finger motion and 100% for right index finger motion.

CHAPTER FIVE

Conclusions and Future Work

This dissertation has presented three wearable antenna designs and their applications in monitoring different human body activities.

First, we designed two FCH antennas, which resonate at 900 MHz and 2.45 GHz. The antenna performance in vicinity of human wrist was simulated and measured, and they show good agreement. Their near field distributions were also simulated. The 900 MHz FCH shows stronger field intensity than the 2.45 GHz FCH antenna.

Then, we designed a low profile wearable Hansen-Woodyard endfire array by using FCH element, which resonates at 2.45 GHz. surface wave propagation along a 1-D FCH array is investigated from both simulation and measurement perspectives. It is found that a backward traveling surface wave can be supported by this structure. The propagation characteristics of this dominant wave mechanism, including its propagation constant and decay constant, were extracted by using the ESPRIT algorithm. The parametric study showed that the wave propagation constant can be controlled by the radius, height of each helix and spacing between adjacent helix. The designed FCH array can achieve a 2.5 dBi gain on chest and 6.25 dBi gain on wrist.

In order to fully integrate wearable antennas into clothing, we explored the possibility to fabricate microstrip antenna by using conductive textiles. After examined most of the conductive textiles available on the market, we selected two conductive textiles, SJ and NC for our study. The DC surface resistivity of both fabrics were studied under different harsh conditions including moisture, perspiration, laundering, taber abrasion, pilling, and wrinkling. It is found that the fabric resistivity could be changed dramatically if they get web by water or sweat. But it will return to normal value after dry. Laundry and wrinkle don't affect the resistivity much. The NC resistivity is changed by 0.05 Ohm. The SJ resistivity is changed by 0.3 Ohm. Pilling causes a severe damage to the fabric conductivity. NC is not functional after the test. A textile patch antenna was designed by using NC fabric, and its performance is comparable to copper antenna thanks to its high conductivity. Similar durability tests were performed on the textile antennas to investigate the harsh wear conditions effect on antenna performance. It is found that wrinkling can slightly cause the antenna gain to drop only by 2 dB. Laundering and moisture can temporarily cause the antenna resonant frequency to shift lower and the gain to drop before antenna is dried, but its performance will return to normal after dry. Pulling the antenna can change its resonance frequency and slightly affect its gain. Pilling could destroy the antenna performance.

The three wearable antennas presented in this dissertation not only can be used for on-body and off-body communications, but also can be used to monitor human body activities by monitoring its input impedance variation. Different human body dynamic experiments have been conducted in the lab, which includes different finger gestures, head and mouth activities and arm motions. For these experiments, the antenna were mounted on wrist, chest, and right side of waist. It is found that different body activities caused the S_{11} different patterns. Dynamic time warping algorithm classification results showed that more than 90% accuracy can be achieved to classify the 4 different finger motions performed in the experiment.

Future research can be extended on the results of above study. For textile antenna, a more thorough study on the laundry effect can be conducted, which may include more wash cycles, more detergents etc. The durability effect on wideband textile antenna performance also needs be investigated, especially its gain and bandwidth. Some novel textile antennas will be designed will fully integration into clothing and new feeding techniques needs to be created for easy integration into clothing. For body dynamic experiment, the number of human subjects needs to be expanded. We will attempt to classify head, mouth and arm motions with different classification algorithms and compare their performance with DTW algorithm.

BIBLIOGRAPHY

[1] Working out shirt. Available: https://www.wearable-technologies.com

[2] http://www.gfk.com/

[3] B. Fang, N. D. Lane, M. Zhang, and F. Kawsar, "HeadScan: a wearable system for radio-based sensing of head and mouth-related activities," 15th IEEE International Conference on Information Processing in Sensor Networks, Austria, 2016.

[4] www.cdc.gov

[5] J.D. Jessen, H. H. Lund, "Playful home training for falls prevention," IEEE International Conference on Advanced Intelligent Mechatronics (AIM), 2015.

[6] ER. Burns, JA. Stevens, R. Lee, "The direct costs of fatal and non-fatal falls among older adults," *Journal of Safety Research*, pp. 99-103, 2016.

[7] Z. Chen, J. T. Kim, J. Liang, J. Zhang, and Y. B. Yuan, "Real-time hand gesture recognition using finger segmentation", *The Scientific World Journal*, Article ID: 267872, 2014.

[8] A. Dubois, and F. Charpillet, "Human activities recognition with RGB-Depth camera using HMM," 35th Annual Intern. Conf. IEEE EMBS, Japan, 2013.

[9] E. Auvinet, F. Multon, A. Saint-Arnaud, J. Rousseau, and J. Meunier, "Fall detection with multiple cameras: an occlusion-resistant method based on 3-D silhouette vertical distribution" *IEEE Transactions on Information Technology in Biomedicine*, vol. 15, pp.290–300, 2011.

[10] P. Gupta and T. Dallas, "Feature selection and activity recognition system using a single tri-axial accelerometer," *IEEE Transactions on Biomedical Engineering*, vol. 61, pp.1780–1786, 2014.

[11] N. Roy, A. Misra, and D. Cook, "Infrastructure-assisted smartphone based adl recognition in multi-inhabitant smart environments," IEEE International Conference on In Pervasive Computing and Communications (PerCom), pp. 38–46, 2013.

[12] C. Xu, P. H. Pathak, and P. Mohapatra, "Finger-writing with Smartwatch: A Case for Finger and Hand Gesture Recognition using Smartwatch," 16th International Workshop on Mobile Computing Systems Applications, pp. 9-14, 2015.

[13] T. Shibano, Y. Ho, Y. Kono, Y. Fujimoto, and T. Yamaguchi, "Daily support system for prevention by using interaction monitoring robot," IEEE International Conference on Intelligent Robots Systems, 2010.

[14] T. Ito, S. Umise, H. Hoshi, M. Suzuki, and S. Tani, "Gait measurement and evaluation system for diagnosis of elderly people's gait condition to prevent fall," International Conference on Advanced Intelligent Mechatronics (AIM), 2015.

[15] Y. Kim and T. Moon, "Human detection and activity classification based on micro-Dopplers using deep convolutional neural networks," *IEEE Geoscience and Remote Sensing Letters*, vol. 13, pp.2-8, Jan. 2016.

[16] https://atap.google.com/soli/

[17] A. Serra, P. Nepa, G. Manara, G. Corsini, and J. L. Volakis, "A single on-body antenna as a sensor for cardiopulmonary monitoring," *IEEE Antennas and Wireless Propagat. Letters*, vol. 9, pp. 930–933, 2010.

[18] Y. Li, and Y. Kim, "Classification of human activities using variation in impedance of single on-body antenna," *IEEE Antennas and Wireless Propagat. Letters*, vol. 16, pp. 541-544, 2016.

[19] C. Baber, J. Knight, D. haniff, and L. cooper, "Ergonomics of wearable computers," *Mobile Networks and Applications*, vol. 4, pp. 15-21, 1999.

[20] O. Shivers, "BodyTalk and the bodynet: a personal information infrastructure, personal information architecture," Cambridge, MA: MIT Laboratory for Computer Science, 1993.

[21] T. Zimmerman, "Personal area netwroks: near field intra-body communications," *IBM Systems Journal*, vol. 35, 1996.

[22] P. Hall, and Y. Hao, "Antennas and propagation for body-centric wireless communications," Artech House, 2006.

[23] G.Z. Yang, "Body sensor networks," Springer, 2006.

[24] J. F. Spratley, P. S. Hall, M. C. Ward, Y. Hao, and A. Alomainy, “Communications for in-body microsensor applications,” *International Workshop on Wearable and implantable Body Area Networks*, Cambridge, 2006.

[25] S. Movassaghi, M. Abolhasan, J. Lipman, D. Smith, and A. Jamalipour, “Wireless body area networks: a survey,” IEEE Communications Surveys & Tutorials, vol. 16, no. 3, pp. 1658-1686, 2014.

[26] P. S. Hall, Y. Hao, Y. I. Nechayv, “Antennas and propagations for on-body communication systems,” IEEE Antennas and Propagation Magazine, vol. 49, no. 3, Jun. 2007.

[27] G. A. Way, W. G. Scanlon, S. L. Cotton and M. J. Bentum, “An analytical path-loss model for on-body radio propagation,” URSI International Symposium on Electromagnetic Theory, pp. 332-335, Aug. 2010.

[28] M. Grimm and D. Manteuffel, “Norton surface waves in the scope of body area networks,” IEEE Transactions on Antennas and Propagation, vol. 62, no. 5, pp. 2616-2613, May 2014.

[29] L. Akhoondzadeh-Asl and P. S. Hall, “Surface wave and creeping waves excitation by body-worn antennas,” Loughborough Antennas and Propagation Conference (LAPC), Loughborough, pp. 48-51, Nov. 2010.

[30] C. Roblin et al., “Antenna design and channel modeling in the BAN context – Part I: Antennas,” *Ann. Telecommun*., vol. 66, no. 3, pp. 139-155, 2011.

[31] M. Abbasi, S. Nikolaou, M. Antoniades, M. Stevanovic, and P. Vryonides, “Compact EBG-backed planar monopole for BAN wearable applications,” IEEE Transactions on Antennas and Propagation, vol. 65, pp. 453-463, 2017

[32] S. Velan, E. Sundarsingh, M. Kanagasabai, A. Sarma, C. Raviteja, R. Sivasamy, J. Pakkathillam, “Dual-band EBG integrated monopole antenna deploying fractal geometry for wearable applications,” *IEEE Antennas and Wireless Propagation Letters*, vol. 14, pp. 249-252, 2015.

[33] S. Kim, Y. Ren, H. Lee, A. Rida, S. Nikolaou, and M. Tentzeris, “Monopole antenna with inkjet-printed EBG array on paper substrate for wearable applications,” *IEEE Antenna and Wireless Propagation Letters*, vol.11, pp.663-666, 2012.

[34] S. Genovesi, F. Costa, F. Fanciulli, and A. Monorchio, “Wearable inkjet-printed wideband antenna by using miniaturized AMC for sub-GHz applications,” *IEEE Antenna and Wireless Propagation Letters*, vol. 15, pp. 1927-1930, 2016.

[35] Z. Duan, D. Linton, W. Scanlon, and G. Conway, “Improving wearable slot antenna performance with EBG structures,” Loughborough Antennas and Propagation Conference, pp. 173-176, 2008.

[36] H. Lee, J. Tak, and J. Choi, “Wearable antenna integrated into military berets for indoor/outdoor positioning system,” IEEE Antennas and Wireless Propagation letters, vol. 16, pp. 1919-1922, 2017.

[37] S. Ha, C. Jung, “Reconfigurable beam steering using a microstrip patch antenna with a u-slot for wearable fabric applications,” *IEEE Antennas and Wireless Propagation Letters*, vol. 10, pp. 1228-1231, 2011.

[38] A. Paraskevopoulos, D. Fonseca, R. Seager, W. Whittow, J. Vardaxoglou, and A. Alexandridis, “Higher-mode textile patch antenna with embroidered vias for on-body communication,” *IET Microwave, Antenna & Propagation*, vol. 10, pp. 802-807, 2016.

[39] K. Furuya, Y. Taira, H. Iwasaki, S. Yamamoto, N. Tamaki, T. Harada, and A. Kuramoto, “Wide band wearable antenna for DTV reception,” in Proc. IEEE Int. Symp. Antennas Propagation, San Diego, 2008.

[40] J. Wang, V. Tripp, “Design of multioctave spiral-mode microstrip antennas,” *IEEE Transactions on Antennas and Propagation*, vol. 39, no. 3, pp. 332-335, 1991.

[41] E.C. Kohls, A. Abler, P. Siemsen, J. Hughes, R. Perez, and D. Widdoes, “A multi-band body-worn antenna vest,” IEEE Antenna and Propagation Society International Symposium, 2004.

[42] D. Paul, C. Jayatissa, G. Hilton, and C. Railton, “Conformability of a textile antenna for reception of digital television,” Loughborough Antennas & Propagation Conference, UK, 2010.

[43] R. W. Adler, D. S. Gibs, J. E. Lebaric, and S. S. Schwarz, “Helmet mounted UHF antenna for mobile user objective system (MUOS),” IEEE International Symposium on Antennas & Propagation, pp. 4176–4179, 2007.

[44] A. Kumar, and R. K. Badhai, “A dual-band on-body printed monopole antenna for body area network,” International conference on Inventive systems and control, 2017.

[45] D. Paul, M. G. Paterson, and G. Hilton, "A low-profile textile antenna for reception of digital television and wireless communications," IEEE Radio and Wireless Symposium, USA, 2013.

[46] D. Paul, H. Giddens, M. G. Paterson, G. Hilton, and J. Mcgeehan, "Impact of body and clothing on a wearable textile dual band antenna at digital television and wireless communications bands," *IEEE Transactions on Antennas and Propagation*, vol. 61, pp. 2188-2194, 2013.

[47] E. F. Sundarsingh, S. Velan, M. Kanagasabai, A. K. Sarma, C. Raviteja, and M. G. N. Alsath, "Polygon-shaped slotted dual-band antenna for wearable applications", *IEEE Antennas and Wireless Propagation Letters*, vol.13, pp. 611-614, 2014.

[48] X. Hu, Y. Sen, and G. Vandenbosch, "Wearable button antenna for dual-band WLAN applications with combined on and off-body radiation patterns," IEEE Transactions on Antennas and Propagation, vol. 65, pp. 1384-1387, 2017.

[49] H. Khaleel, "Innovation in wearable and flexible antennas," Billerica, WIT Press, 2014.

[50] N. Chahat, M. Zhadobov, S. Muhammad, L. Coq, and R. Sauleau, "60 GHz textile antenna array for body-centric communications," IEEE Transactions on Antennas and Propagation, vol. 61, pp. 1816-1824, 2013.

[51] M. Lajevardi, M. Kamyab, "Ultraminiaturized metamaterial-inspired SIW textile antenna for off-body applications," IEEE Antennas and Wireless Propagation Letters, vol. 16, pp. 3155-3158, 2017.

[52] R. Simorangkir, Y. Yang, L. Matekovits, and K. Esselle, "Dual-band dual-mode textile antenna on PDMS substrate for body-centric communications," *IEEE Antennas and Wireless Propagation Letters*, vol. 16, pp. 677-680, 2017.

[53] Y. Hong, J. Tak, and J. Choi, "An all-textile SIW cavity-backed circular ring-slot antenna for WBAN applications," *IEEE Antennas and Wireless Propagation Letters*, vol. 15, pp. 1995-1999, 2016.

[54] https://www.lessemf.com/

[55] T. Koo, D. Kim, J. Ryu, H. Seo, J. Yook, & J. Kim, "Design of a label-typed UHF RFID tag antenna for metallic objects," *IEEE Antennas and Wireless Propagation Letters*, vol. 10, pp. 1010-1014, 2011.

[56] G. Casula, G. Montisci, and G. Mazzarella, "A wideband PET inkjet-printed antenna for UHF RFID," *IEEE Antennas and Wireless Propagation Letters*, vol. 12, pp. 1400-1403, 2013.

[57] H. Khaleel, H. Rizzo, D. Rucker, and S. Mohan, "A compact polyimide-based UWB antenna for flexible electronics," *IEEE Antennas and Wireless Propagation Letters*, vol. 11, pp. 564-567, 2012.

[58] J. Virtanen, T. Bjorninen, L. Ukkonen, and L. Sydanheimo, "Passive UHF inkjet-printed narrow-line RFID tages," *IEEE Antennas and Wireless Propagation Letters*, vol. 9, pp. 440-443, 2010.

[59] S. Nikolaou, G. Ponchak, J. Papapolymerou, and M. Tentzeris, "Conformal double exponentially tapered slot antenna on LCP for UWB applications," *IEEE Transactions on Antennas and Propagations*, vol. 54, pp. 1663-1669, 2006.

[60] G. Dejean, R. Bairavasubramanian, D. Thompson, G. Ponchak, M. Tentzeris, and J. Papapolymerou, "Liquid crystal polymer (LCP): a new organic material for the development of multilayer dual-frequency dual-polarization flexible antenna arrays," *IEEE Antennas and Wireless Propagation Letters*, vol. 4 pp. 22-26, 2005.

[61] S. Sangaralingam, B. Gupta, "Determination of dielectric constant of fabric materials and their use as substrates for design and development of antennas for wearable applications", *IEEE Transactions on Instrumentation and Measurement*, vol. 59, pp. 3122-3130, 2010.

[62] S. Best, "A comparison of the cylindrical folded helix Q to the Gustafsson limit," in Proc. EuCAP, Berlin, Germany, pp.2554–2557, Mar. 2009.

[63] https://www.feko.info/

[64] A. Paulraj, R. Roy and T. Kailath, "Estimation Of Signal Parameters Via Rotational Invariance Techniques- Esprit," 19th Asilomar Conference on Circuits, Systems and Computers, pp, 83-89, 1985.

[65] Y. Li, and H. Ling, "Extraction of Wave Propagation Mechanisms in a Cut-Wire Array Using the ESPRIT Algorithm," *IEEE Antennas and Wireless Propagation Letters*, vol. 8, pp: 744-747, 2009.

[66] D. Xue and Y. Li, "Design of a closely-spaced, multiple-element parasitic antenna array," *Microwave Optical Technical Letters*, vol. 56, no. 10, pp. 2374-2377, Oct. 2014.

[67] Z. Bayraktar, P.L. Werner, and D. H. Werner, “The design of miniature three-element stochastic Yagi-Uda arrays using particle swarm optimization”, *IEEE Antennas and Wireless Propagation Letters*, vol. 5, pp. 22–26, 2006.

[68] S. Lim and H. Ling, “Design of electrically small, pattern reconfigurable Yagi antenna”, *Electronics Letters*, vol. 43, pp: 1326–1327, 2007.

[69] J. Yu, Y. Le and S. Lim, “Design of a Dual-Band, Electrically Small, Parasitic Array Antenna,” *IEEE Antennas and Wireless Propagation Letters*, vol. 13, pp: 1453-1456, 2014.

[70] D. Arceo and C.A. Balanis, “A Compact Yagi-Uda Antenna with Enhanced Bandwidth”, *IEEE Antennas and Wireless Propagation Letters*, vol. 10, pp: 442–445, 2011.

[71] https://www.cst.com/

[72] Z. Wang, L. Lee, D. Psychoudakis, and J. Volakis, “Embroidered Multiband Body-Worn Antenna for GSM/PCS/WLAN Communications”, *IEEE Transaction on Antennas Propagations*, vol. 62, pp. 3321-3329, 2014.

[73] R. Parashkov, E. Becker, T. Riedl, H. Johannes, and W. Kowalsky, “Large Area Electronics Using Printing Methods”, *IEEE Proceedings*, vol. 93, pp. 1321-1329, 2005.

[74] S. Yang, P. Soh, and G. Vandenbosch, “Dual-Band Textile MIMO Antenna based on Substrate-Integrated Waveguide (SIW) technology”, *IEEE Transaction on Antennas Propagations*, vol. 63, pp. 4640-4647, 2015.

[75] C. Hertleer, A. Laere, H. Rogier, and L. Langenhove, “Influence of Relative Humidity on Textile Antenna Performance”, *Textile Research Journal*, vol. 80, pp. 177-183, 2009.

[76] P. Salonen, M. Keskilammi, and Y. Samii, “Textile Antennas: Effects of Antenna bending on Radiation Pattern and Efficiency”, Antennas and Propagation Society International Symposium, 2008.

[77] P. Salonen, Y. Samii, “Textile Antennas: Effects of Antenna Bending on Input Matching and Impedance Bandwidth”, *IEEE Aerospace and Electronic Systems Magazine*, vol. 22, pp. 10-14, 2007.

[78] Branimir I., Goran, G., and Davor, B., “Performance of Wearable Antenna Exposed to Adverse Environmental Conditions”, 21st International Conference on Applied Electromagnetics and Communications, 2013.

[79] AATCC standards: https://www.aatcc.org/

[80] Sumsuang: https://www.samsung.

[81] J. Aggarwal and Q. Cai, “Human motion analysis: A review,” *Computer Vision and Image Understanding*, vol. 73, pp. 428–440, 1999.

[82] Google soli project: https://atap.google.com/soli/

[83] Y. Kim and B. Toomajian, "Hand gesture recognition using micro-Doppler signatures with convolutional neural network," *IEEE Access*, pp. 1-5, Iss. 99, 2016.

[84] ASTM Standards: https://www.astm.org

[85] Bin Xu, Yang Li, “Backward surface wave propagation and radiation along a one-dimensional folded cylindrical helix array”, *International Journal of Antennas and Propagation*, Article ID 210254, 2015.

[86] Bin Xu, Yang Li, and Youngwook Kim, “Classification of finger movements based on reflection coefficient variations of a body-worn electrically small antenna,” *IEEE Antennas and Wireless Propagation Letters*, vol. 16, pp: 1812 -1815, March, 2017. DOI: 10.1109/LAWP.2017.2681099.